Optical, thermal, electrical, damage, and phase-matching properties of lithium selenoindate

Valentin Petrov,[1,*] Jean-Jacques Zondy,[2] Olivier Bidault,[3] Ludmila Isaenko,[4] Vitaliy Vedenyapin,[4] Alexander Yelisseyev,[4] Weidong Chen,[5] Aleksey Tyazhev,[1] Sergei Lobanov,[4] Georgi Marchev,[1] and Dmitri Kolker[6,7]

[1]*Max-Born-Institute for Nonlinear Optics and Ultrafast Spectroscopy, 2A Max-Born-Str., D-12489 Berlin, Germany*
[2]*Laboratoire Commun de Métrologie LNE-Cnam, 61 rue du Landy, 93210 La Plaine Saint Denis, France*
[3]*I.C.B., CNRS–Université de Bourgogne, 21078 Dijon, France*
[4]*Institute of Geology and Mineralogy, SB RAS, 43 Russkaya Str., 630058 Novosibirsk, Russia*
[5]*Laboratoire de Physicochimie de l'Atmosphère (UMR-CNRS 8101), Université du Littoral Côte d'Opale,*
145 Av. Maurice Schumann, F-59140 Dunkerque, France
[6]*Novosibirsk State Technical University, 20 K. Marx Pr., Novosibirsk 630072, Russia*
[7]*Institute of Laser Physics (SB-RAS), 13/3 Lavren'teva Pr., Novosibirsk 630090, Russia*
*Corresponding author: petrov@mbi-berlin.de

Lithium selenoindate ($LiInSe_2$) is a new nonlinear chalcogenide biaxial crystal, related to $LiInS_2$ and transparent from 0.54 to 10 μm at the 50% level (10 mm thickness), which has been successfully grown in large sizes and with good optical quality. We report on what we believe to be new physical properties that are relevant for laser and nonlinear optical applications and summarize all relevant characteristics, both from the literature and as measured in the present work. With respect to $AgGaS(e)_2$ ternary chalcopyrite materials, $LiInSe_2$ displays a nearly isotropic thermal expansion behavior with three- to five-times-larger thermal conductivities associated with high optical damage thresholds, and low intensity-dependent absorption, allowing direct high-power downconversion from the near-infrared, especially 1064 nm, to the deep mid-infrared. Continuous-wave difference-frequency generation (5.9−8.1 μm) of Ti:sapphire laser sources is reported for the first time as well as nanosecond optical parametric oscillation with a Nd:YAG laser as the pump source at 100 Hz and idler tuning between 4.7 and 8.7 μm. © 2010 Optical Society of America

OCIS codes: 190.4400, 190.4410, 190.4970.

1. INTRODUCTION

To date, only a few suitable nonlinear crystals combining a transparency extending into the mid-infrared (mid-IR) range above ~5 μm (the upper limit of oxide materials) and large-enough birefringence to permit phase-matching over their transparency ranges are available. The binary and ternary birefringent noncentrosymmetric crystals now in use in this spectral region include the chalcopyrite semiconductors $AgGaS_2$ (AGS), $AgGaSe_2$ (AGSe), $ZnGeP_2$ (ZGP) and $CdGeAs_2$ (CGA), the defect chalcopyrite $HgGa_2S_4$ (HGS), GaSe, CdSe, and Tl_3AsSe_3 (TAS) [1]. Some other crystals like proustite (Ag_3AsS_3) and pyrargyrite (Ag_3SbS_3) have already lost their importance because they were completely replaced with the more technological AGS while the growth technology of HgS was never developed [2]. The list of the non-oxide birefringent inorganic crystals ever used will be full if the elemental Se and Te are added: Their linear losses are, however, so high that at present they could be interesting (especially Te) only for diagnostic purposes of short pulses at longer wavelengths [2]. All these mid-IR crystals are uniaxial. All of them that are now available commercially or quasi-commercially (from laboratories) have not only their specific advantages but also some drawbacks: AGS and AGSe have low residual absorptions but poor thermal conductivities and anisotropic thermal expansions with different signs; ZGP has excellent nonlinearity and thermal conductivity, but multi-phonon and residual absorption limit its transparency from both sides so that pump wavelengths should lie above 2 μm which corresponds to less than 1/3 of its bandgap; CGA possesses extremely high nonlinearity but exhibits also absorption features, and low temperatures are required to avoid the residual losses; HGS has a very high nonlinear figure of merit but its growth technology is very difficult and only small sizes are available; GaSe has large nonlinearity and birefringence but it is a soft cleaving compound, with very low damage threshold; CdSe is transparent up to 18 μm but its birefringence and nonlinearity are quite modest; TAS exhibits rather low losses in its transparency range but its thermal conductivity is extremely low; and finally Te is a unique nonlinear material having in mind its extended wavelength range and superior nonlinear susceptibility, but as already mentioned its applicability is limited by the high linear losses. Finally, a new chalcopyrite still in its development stage, $CdSiP_2$ (CSP), should be mentioned because it not only showed some very attractive properties but already found some applications [3].

Two approaches to develop alternative solutions and avoid the above mentioned drawbacks in specific applications include the manufacturing of quasi-phase-matched orientation patterned structures with highly nonlinear but isotropic semiconductors, e.g., GaAs which has a mature technology [4], and the doping or mixing of nonlinear

crystals to produce more complex ternary compounds like GaS_xSe_{1-x} [5] or quaternary compounds like $AgIn_xGa_{1-x}S(e)_2$, $Cd_xHg_{1-x}Ga_2S_4$, and $Ag_xGa_xGe_{1-x}S(e)_2$ [6,7]. The problems with them are the limited thickness in the former case and the homogeneity of the composition in the latter.

In the last decade, considerable progress has been made with two orthorhombic ternary chalcogenides, $LiInS_2$ (LIS) and $LiInSe_2$ (LISe), whose growth technology was improved to such an extent that it was possible to perform extensive characterization and even realize some applications [8]. Both not only proved to be useful for the mid-IR spectral range but also possess some unique properties which will definitely guarantee them a place among the other mid-IR nonlinear crystals if some technological issues are developed to an end. Moreover, their attractive features already stimulated the study of further crystals belonging to the same class like $LiGaS_2$, $LiGaSe_2$, and $LiGaTe_2$ which are now also under development [9–11].

The optical, vibrational, thermal, electrical, damage, and phase-matching properties of the sulfide compound LIS were summarized in a review paper [12]. The present paper is a continuation of this work, devoted to the closely related LISe and focusing on its optical, thermal, electrical, damage, and phase-matching properties, as well applications in various downconversion nonlinear optical processes.

2. GROWTH, COMPOSITION, AND STRUCTURE

LISe is a congruently melting compound and can be grown from the melt using the three elements as starting materials. In the first report on LISe by Negran *et al.* [13], the crystalline samples grown by directional freezing in graphite crucibles were deep red in color. This work identified the symmetry class as $mm2$. Kamijoh and Kuriyama grew single crystals of LISe of about ϕ10 mm $\times$20 mm, again deep red in color, also by directional solidification with a temperature gradient of 4°C/cm at a cooling rate of 2°C/h [14]. They determined a melting temperature of 904°C for LISe and estimated the lattice constants.

A yellow phase of LISe with the same structure was mentioned for the first time in [15] where the photoluminescence properties were compared to those of the red phase. Yellow-brownish LISe crystals as large as ϕ10 mm$\times$20 mm were obtained by directional solidification in [16]. The melting temperature was determined to be 897°C. The LISe growth parameters used for the directional solidification and vertical Bridgman–Stockbarger methods were described in [17]. The red coloration was associated with a shift toward In_2Se_3 along the binary cross-connection $Li_2Se-In_2Se_3$ of the compositional triangle Li–In–Se [17]. The yellow phase is closer to the ideal stoichiometric composition. Annealing of the yellow phase in vacuum did not change the color but annealing in Se-atmosphere resulted in color transformation to red [17]. An excess of Li and Se was required in order to compensate the loss during the growth process [14,16,17]. The phase diagram of the system $Li_2Se-In_2Se_3$ was studied in [17,18].

Badikov *et al.* [19] grew LISe by the vertical Bridgman–Stockbarger technique starting with In_2Se_3, Li, and Se and achieving crystal sizes of ϕ18 mm$\times$50–60 mm. They determined melting temperature of 920°C for LISe and reported also the lattice constants. Finally, the isostructural mixed compound LiInSSe, which can be regarded as a solid solution $LiIn(S_{1-x}Se_x)_2$ for $x=0.5$, was also successfully grown by the same method achieving similar sizes [20,21].

We use a seeded Bridgman–Stockbarger process in a vertical two-zone furnace with counterpressure to grow large size single-crystal ingots of LISe. Details on the growth procedure can be found elsewhere [22]. In principle, the synthesis and growth of LISe follow the same procedure as that for growing chalcopyrites, except for some refinements related to the volatility of the elements and the chemical reactivity of Li with the container walls. The purity of the starting materials is 99.999% (In, Se) and 99.9% (Li). Se is additionally purified by sublimation in vacuum while the metals are subjected to repeated zone melting and directional crystallization. Since the most volatile component, Se, has a high partial pressure at the temperature of the LISe pyrosynthesis, the latter is carried out in a two-zone furnace to avoid the container explosion. The temperature of the "hot" zone, in which the crucible with the reaction mixture is placed, is 50°C–100°C higher than the melting temperature of the crystal. Our updated value for the melting temperature of LISe is 915°C±5°C, which lies between the values specified by others [14,16,19,23].

The temperature of the "cold" zone is selected in such a way that the vapor pressure does not exceed 2 atm. The synthesized compound is placed into a glass-carbon ampoule which is in turn mounted inside a sealed silica ampoule of larger diameter filled with dry Ar (0.5–1 atm). The inner ampoule is necessary to prevent the outer quartz tube from reaction with Li. Such a double-wall growth ampoule containing the polycrystalline synthesis charge and a seed is placed in the furnace so that the charge and the upper portion of the seed are melted. A temperature gradient of 10°C/cm–15°C/cm is sufficient to maintain a stable growth interface in the furnace. Growth is accomplished by moving the melt interface slowly from the seed. The ampoule is shifted at a rate of 1–10 mm/day. Initially we used (010) and (001) oriented seeds. However, since the thermal expansion of LISe is almost isotropic, in contrast to AGS and AGSe, the present state of the art enables the use of any seed orientation in order to grow sufficiently large crystals along the required phase-matching directions. Single-crystal ingots obtained can be as large as 30 mm in diameter and 100 mm in length (Fig. 1). They are free of extended defects as inclusions, twins, cracks, etc.

In order to improve the synthesis conditions for stoichiometric growth, the LISe evaporation process was studied using a unique thermo-microscopic technique [22,24,25]. It became clear that possible deviations from the stoichiometric composition of LISe may occur both in the synthesis stage and during the crystal growth [26,27]. Thus, the starting composition of the charge must compensate for the loss of Li and Se, the vapor of which interacts with the silica reactor. During growth, the specific character of the
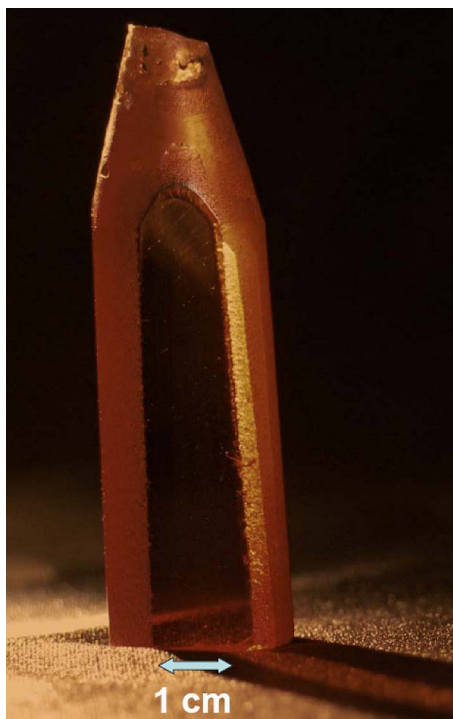
Fig. 1.   (Color online) LiInSe$_2$ boule grown by the Bridgman–Stockbarger technique on oriented seed. The sample was annealed in vacuum after growth to improve the transparency. After annealing the crystal composition is stoichiometric.

T-x diagram for the Li$_2$Se−In$_2$Se$_3$ system has to be taken into account, where the melt laminates into two fluids of different compositions at temperatures above 938°C (the monotectics temperature), both enriched in Li$_2$Se [25]. It was established that the LISe compound melts incongruently under the equilibrium pressure of its own vapor which amounts to about 0.05 atm, but evaporation of the LISe melt is congruent because of preferable evaporation of the In$_2$Se$_3$ molecules. Thus there may be a shift of the melt composition to the Li$_2$Se side and this shift depends on temperature/temporal regime, free space, and the Ar pressure inside the reactor ampoule.

Excess melt superheating as well as long superheating time may cause crystallization to occur from the inhomogeneous part of the liquid. In this case Li$_2$Se clusters accumulated at the crystallization front end up in the crystal and appear as small size inclusions. It is difficult to achieve the optical quality of the polished faces of such crystals because these inclusions are highly hygroscopic. Thus, superheating and evaporation should be minimized. This is possible when the Ar pressure inside the ampoule (reactor) is about 1 atm and the melt superheating does not exceed 20°C−30°C. In such cases the composition shift is below 1 mol % and the crystal grows from homogeneous melt free of small size hygroscopic inclusions of Li$_2$Se.

Point defects in LISe were studied by photoluminescence [15], optical absorption [28,29], and nuclear magnetic resonance [27,30]. Point defects determine the crystal color through their absorption bands which are affected by the annealing procedure. Analysis of nuclear magnetic resonance spectra, along with x-ray diffraction

and optical spectroscopy data, indicates that the change in color upon annealing in In$_2$Se$_2$ vapor is due to a change in the number of point defects [30].

A detailed structural analysis of LISe was performed by Hönle *et al.* [31]. The lattice parameters reported were for single crystals of brown color. The structure of LISe is formed by LiSe$_4$ and InSe$_4$ tetrahedrons, and the Se^{2-} ions are arranged in hexagonal packing with tetragonal and octahedral cavities (tetrapores and octapores; Fig. 2). The β-NaFeO$_2$ structure (space group $Pna2_1$ or C_{2v}^9) is less dense than the chalcopyrite structures of AGS and AGSe due to the presence of these empty cavities in the unit cell volume. Only half of the tetrapores are occupied by Li and In while all octapores are empty. The spontaneous polarization is due to the fact that in each bipyramid formed by two adjacent tetrapores only one is occupied by a cation. The unit cell parameters of LISe are roughly a = 7.2 Å, b = 8.4 Å, and c = 6.8 Å [28]. The exact lattice parameters depend on the coloration, i.e., on the growth and annealing conditions and the exact stoichiometry, but the structures of all LISe crystals are the same [28].

No phase transformation has been detected in LISe up to the melting point [31] but thermal decomposition in vacuum was observed starting from 750°C−790°C [17,32]. Aging of the surface layer of both red and yellow phase LISe was studied in [17] and attributed to reactions involving lithium. Structural phase transitions under pressure at room and elevated temperatures were investigated in [33–38].

A comparison of the effective charges of the Li–Se and In–Se bonds [39] suggested that the electrons in the Li–Se bond are more tightly bound to the anion than in the In–Se bond. Analyzing spectroscopic data it was possible to conclude that the Li–Se bonds in LISe are essentially ionic in nature and the structural properties (stability of the β-NaFeO$_2$ structure) can be understood in terms of the average bond parameters [40].

The electronic structure of LISe was first studied in [41]. Several first principles calculations appeared more recently [42–45] in which the effect on some optical properties (through the dielectric constant) is also analyzed.
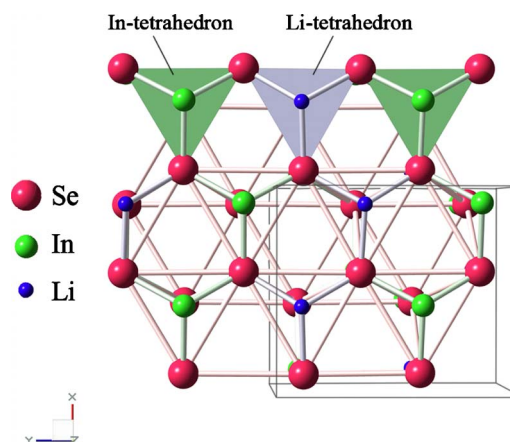

Fig. 2.   (Color online) The orthorhombic unit cell structure of LISe: the box frame gives the orientation of the unit cell.

3. BANDGAP, TRANSMISSION, AND VIBRATIONAL PROPERTIES

For red color LISe samples, the first estimation of the energy bandgap from optical transmission was 1.88 eV at room temperature [14]. A value of 2 eV is found in [23]. Several other works dealt with the bandgap at low and room temperatures. Similar results were obtained from photoluminescence [15] and electrical resistivity [46] measurements and were confirmed from electronic structure calculations [41]. A slightly lower value (1.6 eV) was obtained from diffuse reflectance [47] measurements. Further optical absorption measurements indicated indirect nature of the bandgap and weak polarization dependence [48]. The updated bandgap value of 2.03 eV measured with yellow color LISe was attributed to indirect or pseudo-direct transitions [33], but for a thickness of 4 μm a direct absorption edge near 2.9 eV was also identified in this work.

Obviously the experimental results depend on the color of the samples used, i.e., on the point defects present. Transmission measurements with yellow color LISe indicated a direct transition [16,17,49,50] with a bandgap very close to our updated value of 2.86 eV at room temperature [27,28]. The polarization dichroism is again weakly pronounced [28]. First principles calculations still lead to lower values of this direct bandgap [43–45], e.g., 2.63 eV in [45].

Transmission spectra of LISe were measured both for yellow and red colorations [19,27–29,51,52]. They revealed independence of the IR cutoff edge from the color. The long-wave limit for the clear transparency does not extend significantly further into the mid-IR in comparison to LIS [27,28,51]. Aging of the surfaces can strongly affect the crystal transmission, especially in the visible [17,49].

Absorption coefficient of less than 0.05 cm^{-1} was specified near 1 μm for some special samples [19] but loss coefficients of <0.1 cm^{-1} in the clear transmission range, and 0.55 and 1.2 cm^{-1} at 9.55 and 10.6 μm, respectively, were also given in the literature [51,52]. The variation of the transmission at different points of the sample surface did not exceed 2% [52,53]. The transmission of LiInSSe extends to roughly 13.7 μm at the "zero"-level and also shows the characteristic dip at 10 μm [20,21], like for LISe (see Fig. 3).

In Fig. 3 we present new polarized measurements of the transmission with state of the art samples of LISe. A sufficient thickness (10.5 mm) is chosen in order to visualize the potential for real applications. Here and further on X, Y, and Z denote the principal optic axes which will be identified in Section 6. The thin lines show the limits set by the Fresnel reflections (with consideration of multiple reflections). The measurements indicate that the 50% transmission level extends from 0.54 to 10 μm while the clear transparency range is roughly from 1 to 8 μm. Nevertheless, thin samples of LISe, e.g., as required for femtosecond frequency conversion, could be used also for longer wavelengths, up to ~12 μm. The absorption losses vanish around 6 μm (see Fig. 3). At 1.064 μm they are 2%/cm. This is much less than the 6.5%/cm–20.8%/cm derived previously from calorimetric measurements with older samples [54–56] which are contradictory and obviously affected by surface aging and absorption.
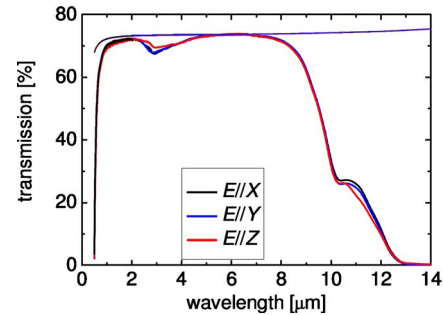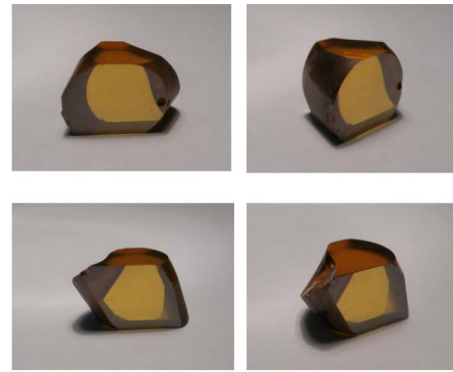

Fig. 3. (Color online) Polarized transmission spectra of LISe for a thickness of 10.5 mm. The boule used was grown by the vertical Bridgman–Stockbarger method using an oriented seed and annealing in vacuum was applied to achieve stoichiometric composition. The photographs show the X-cut (above) and Z-cut (below) samples used.

Infrared (IR) reflectivity and Raman spectra with polarized light were recorded for yellow phase LISe at room and low temperatures in [17,50,57]. With the complementary information from IR and Raman spectroscopy, the observed 33 IR active and the 12 exclusively Raman active modes could be assigned to their corresponding symmetry classes; tabulations can be found in [17,57]. No difference was observed between the red and yellow phases [17]. As expected from reduced mass considerations the optical mode frequencies of LISe are shifted to lower frequencies in comparison to LIS [12] due to the substitution of sulfur by selenium. The dominant line of the total symmetrical A_1 mode lies at 268 cm^{-1} for LIS and at 161.5 cm^{-1} for LISe [57]. The ratio of 1.66 of the frequencies of these lines corresponds to the square root (1.57) of the ratio of the atomic masses of selenium and sulfur. From absorption features of the transmission spectra and the maximum phonon energy of LISe (375 cm^{-1}), it can be concluded that the onset of absorption near 10 μm is due to three-phonon absorption and the cutoff edge is set by two-phonon absorption. The fact that the IR-cut cutoff edge of LISe is not substantially extended in comparison to LIS can be explained by the role of the Li–S(e) sublattice vibrations while in AGS and AGSe, in the presence of the much heavier Ag ion, the high-frequency vibrations are related to the Ga–S(e) sublattice. Theoretical calculations of the lattice dynamics in LISe can be found in [44], and Raman spectra recorded at high pressure were analyzed in [37,38].

4. THERMAL AND THERMO-OPTIC PROPERTIES

The thermal properties of a new nonlinear optical material are crucial in assessing its potential in real nonlinear conversion devices pumped by high-power continuous-wave (CW) or pulsed lasers. The performance of devices based on mid-IR chalcogenides is often limited by deleterious thermal effects (lensing and expansion). The thermal figure of merit of a material can be defined as $(\mathrm{d}n/\mathrm{d}T)/K$, where $\mathrm{d}n/\mathrm{d}T$ is the thermo-optic index variation and K is the thermal conductivity. The larger is this quantity, the more severe are the thermal limitations. The figure of merit enters the expression for the focal length of the thermal lens in a nonlinear crystal, $f = \pi w_0^2 K/[\alpha l P(\mathrm{d}n/\mathrm{d}T)\ln 2]$, where α is the absorption coefficient at the pump wavelength, l is the crystal length, P is the pump power, and w_0 is the pump beam radius. A second thermal quantity $t_D = w_0 C_p/4K$, where C_p is the mass specific heat of the material, gives the characteristic time of heat diffusion outside the pumped volume. According to the definition of the heat capacity C_p, the increase in crystal energy at heating is $\Delta E = C_p \Delta T$, where ΔT is the temperature increment due to the heat absorption. For a crystal with a large heat capacity, when it absorbs light energy and increases its thermal energy, the temperature gradient is small. This means that heat capacity is one of the important factors that influence the damage threshold of a crystal. The larger is the diffusion time t_D, the stronger are the thermal lensing effects. Hence it is important to know C_p, K, and $\mathrm{d}n/\mathrm{d}T$. In addition the thermo-optic coefficients are needed to predict the temperature dependence of the phase-matching performance in $\chi^{(2)}$ interactions.

A. Specific Heat at Constant Pressure

The general theoretical expression for $C_p(T)$ of anharmonic solids is

$$C_p(T) = 12R\left[F(x_D) + \sum_{k=1}^{N} c_k T^k \right], \qquad (1)$$

where R is the molar gas constant, $x_D = T_D/T$ (T_D is the Debye temperature), and $F(x_D)$ is the Debye function describing the temperature dependence in the harmonic lattice vibration approximation,

$$F(x_D) = \frac{3}{x_D^3} \int_0^{x_D} \frac{x^4 e^x \mathrm{d}x}{(e^x - 1)^2}. \qquad (2)$$

The Debye temperature can be estimated independently from the melting temperatures and lattice parameters using the modified Lindemann formulas applied to the case of $A^I B^{III} C_2^{VI}$ compounds [58]: $T_D = 238$ K according to our estimation or 240 K according to [59]. These T_D values correspond to sufficiently low temperatures when only low-energy phonons are excited and the Debye model is valid. The high-temperature limit of the Debye temperature T_D^∞ can be obtained from the maximum energy of the vibrational spectrum: $kT_D^\infty = \hbar\omega_{\max}$, where k and $\hbar$ are the Boltzmann and Planck constants, respectively, and $\omega_{\max}$ is the maximum frequency of crystal vibrations and all possible vibrations are excited. Taking $\omega_{\max}$ from Ra-

man and/or IR reflectivity spectra as 360 cm^{-1} (≈ 0.045 eV) [57], one arrives at $T_D^\infty = 518$ K.

Two unoriented samples of LISe, which were 57.91 mg in weight (sample A) and 86.05 mg in weight (sample B), prepared as 1.2 mm high cylinders were cut from single crystals of yellow color for the specific heat measurements. Heat capacity measurements were performed with a differential scanning calorimeter DSC-204 Netzsch in the temperature range of 113–483 K. A single crystal of Al_2O_3, 66.45 mg in weight, was used for the calibration as a reference sample. More details about the experimental procedure can be found in [60].

The measured heat capacity of LISe versus temperature in the 170–470 K range is shown in Fig. 4. The error is estimated to be 1–2.5 J mol^{-1} K^{-1}, depending on sample and temperature. The experimental results fit the function

$$C_p = 114.02 - 5708T^{-1} - 187\,540T^{-2}, \qquad (3)$$

with T in kelvin: the deviations are less than ±0.35 J mol^{-1} K^{-1} (Fig. 4). The harmonic contribution $c_{\mathrm{ph}} = 12RF(x_D)$ to $C_p(T)$ is also plotted in Fig. 4 and a cross point between c_{ph} and C_p occurs at 270 K similarly as in the case of LIS [60]. As can be seen from Fig. 4 our value of C_p at room temperature (98.1 ± 1.4 J mol^{-1} K^{-1}) is in good agreement with previous results obtained using red polycrystalline LISe, 96 ± 1 J mol^{-1} K^{-1} [59,61], measurements that were performed between 200 and 550 K and between 2 and 300 K, respectively. We conclude that the heat capacity does not depend on the sample coloration contrary to the observations in [17] where the heat capacity of yellow LISe was estimated to be about 5% lower than that of red color LISe in the 400–510 K temperature range.

The value of N and the absolute values of c_k in Eq. (1) are a measure of the degree of lattice anharmonicity. $N = 4$ and 1 order of magnitude higher c_k values in comparison to the $A^I B^{III} C_2^{VI}$ chalcopyrites [59] show that $LiInC_2^{VI}$ compounds have much larger anharmonic contribution. This is a result of the specific nature of the $Li-C^{VI}$ bond, which—as already mentioned—is weaker than the $In-C^{VI}$ bond. It is worthwhile noting that due to the heavier atoms in its structure and the related larger C_p,
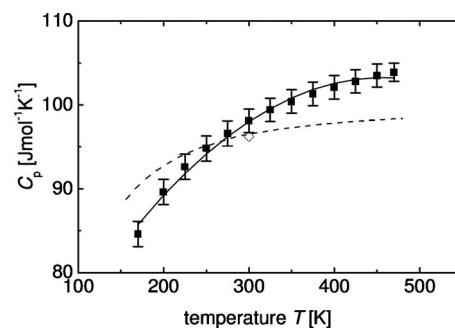

Fig. 4.   Measured heat capacity of LISe versus temperature (squares and error bars) and fitting results (solid curve). The C_p value previously measured for red polycrystalline LISe (diamond), taken from [59], is also shown. The dashed line is based on the harmonic term $c_{\mathrm{ph}}(T)$ in expression (1), with a Debye temperature of $T_D = 240$ K.

the LISe crystal is expected to have lower temperature gradients under laser beam irradiation than LIS.

Gmelin and Höhnle [61], who studied the molar heat capacity at low temperatures from 2 to 300 K, found an excess heat below ~80 K and explained it as a two level Schottky anomaly with an energy splitting of ΔE =0.006 eV or $\Delta E/k$=71.4 K. They suggested that the Li atoms can reside in a double-well potential with some energy barrier between them. These two possible Li positions may correspond to different directions of the spontaneous polarization vector in the pyroelectric LISe crystal, and the characteristic temperature (71.4 K) means that LISe becomes ferroelectric only at yet lower temperatures ($T<71.4$ K). Ferroelectricity of LISe is of great importance for the fabrication of periodic structures and the realization of quasi-phase-matching. However, attempts to reverse the spontaneous polarization by the application of electric field were unsuccessful at room temperature [13], while the possibility of an existing ferroelectric phase has been disproved above room temperature from the result of differential thermal analysis [14] and also down to 77 K from capacitance measurements of the dielectric constant [62].

B. Thermal Conductivity

For thermal conductivity and expansion measurements we cut and polished three cylinders from red color LISe with identical diameter and length, both equal to 5 mm, and with their axes parallel to one of the crystallographic (optical) axes. The thermal conductivity of LISe was measured in the 293–343 K temperature range under the monotonic heating regime using a $C\lambda$-calorimeter [60,63]. The whole equipment was tested and calibrated with fused silica. The experimental error was estimated to be ±6%. The temperature dependence of the results obtained could be fitted by the linear expressions

$$K_X = 6.739 - 0.00668T,$$

$$K_Y = 7.70 - 0.0101T,$$

$$K_Z = 8.539 - 0.0103T, \tag{4}$$

where T is in kelvin and the conductivity K is in W m^{-1} K^{-1}.

A typical temperature dependence of the thermal conductivity $K(T)$ for insulators exhibits a peak with its maximum located at about half the Debye temperature T_D with $K\sim T^3$ and $K\sim T^{-1}$ at lower and higher temperatures, respectively [64]. The negative slopes of the $K(T)$ dependence in Eqs. (4) show that our measurements were carried out at temperatures exceeding the peak maximum ($T_D/2$). Taking into account that $T_D\sim 240$ K for LISe [59] (see the previous subsection), the peak position is estimated to be at $T_{max}\sim 120$ K, which is indeed below the experimental temperatures, 293–343 K. The values we obtained at room temperature (300 K), K_X=4.74± 0.25 W m^{-1} K^{-1}, K_Y=4.68±0.25 W m^{-1} K^{-1}, K_Z=5.46± 0.32 W m^{-1} K^{-1}, are roughly 25% lower than those known for LIS [12]; they are still, however, three to five times larger than for AGS and AGSe crystals [60,63]. The room temperature values were confirmed in an independent

measurement at Cleveland Crystals [8], which gives us confidence in their reliability. We have, however, no explanation for the large discrepancy with the results in [20,52] where a value of $K=1.4\pm0.2$ W m^{-1} K^{-1} can be found for LISe.

In insulators, phonons are responsible for the transfer of the thermal motion energy. The lower maximum phonon energy which is related to the Li–Se vibrations explains the slightly lower thermal conductivity of LISe in comparison to LIS where the lighter chalcogen (S) results in higher maximum phonon energies (see Section 3). The presence of the heavier metal (Ag) in AGS and AGSe explains their substantially lower thermal conductivities.

C. Thermal Expansion

The anharmonicity of atom vibrations in the crystal lattice is the main reason for thermal expansion in solids. The linear expansion coefficients of LISe, $\alpha=(1/l)\mathrm{d}l/\mathrm{d}T$, were measured in the 300–450 K temperature range with the same samples as in the previous subsection using a thermo-mechanical analyzer TMA-202 Netzsch. Changes in the sample length were determined at temperature increments of +15 and −15 K (heating and cooling at a scanning rate of 6 K/min). Each step of temperature change was followed by an isothermal interval of about 20 min to attain temperature equilibrium. The same experimental procedure was used for the measurements of a reference sample: an aluminum (Al) cylinder of 6 mm diameter and 5 mm height. Three measurement runs for each sample were carried out, with only one run at once. The measurement order of the samples was random to avoid any trend in the experimental results which are summarized in Table 1.

Our direct measurements can be compared to estimations based on the measurements of the LISe lattice constants in the range 303–773 K [17], assuming no temperature dependence of α_i, which seems to be justified having in mind the results in Table 1. The reported in [17] values α_X=19.8×10^{-6} K^{-1}, α_Y=9.36×10^{-6} K^{-1}, and α_Z=6.4 ×10^{-6} K^{-1} show slightly stronger anisotropy but are in reasonable agreement with our results.

The results of our measurements were fitted to a polynomial law $A+BT+CT^2$. The accuracy of the final values $\alpha(T)$ was estimated as the mean square deviation of experimental points from the fitting function in a temperature interval of 50 K. The uncertainties for $\alpha_X(T)$, $\alpha_Y(T)$, and $\alpha_Z(T)$ include the uncertainty for the results in the Al reference sample measurements. The results of the polynomial fitting are

$$\alpha_X = 7.0 + 0.0463T - 36.7 \times 10^{-6}T^2,$$

Table 1. Linear Thermal Expansion Coefficients α_i (10^{-6} K^{-1}) of LISe

T (K)	α_X	α_Y	α_Z
300	17.6±1.8	11.0±1.6	8.7±1.1
350	18.7±2.1	10.2±1.9	9.0±1.6
400	19.7±1.7	10.0±1.0	9.1±1.4
450	20.4±2.4	11.5±1.7	8.9±2.4

$$\alpha_Y = 30.3 - 0.1051T + 135.9 \times 10^{-6}T^2,$$

$$\alpha_Z = 1.0 + 0.0417T - 53.8 \times 10^{-6}T^2, \qquad (5)$$

where T is measured in kelvin and α_i in 10^{-6} K^{-1}.

The α_i values measured for LISe at room temperature are comparable to those of LIS [60,63]. Although similar in absolute value to the uniaxial chalcopyrite compounds (AGS and AGSe; see [60,63]), in contrast to the latter, the expansion coefficients of LISe (like those of LIS) have the same sign along different crystallographic (optical) directions, which is not the case for the chalcopyrite structure. This property is of great importance for crystal growth and surface coating: it is easier to avoid ampoule cracking when growing crystals and to ensure good mechanical stability of dielectric coatings.

D. Thermo-optic Coefficients
Two prisms with different orientations and optically polished faces were manufactured from yellow LISe for the measurement of the thermo-optic coefficients. Characteristic dimensions were 6 mm height and $\approx$9 mm side edges of the isosceles triangle in the prism base. The accuracy of orientation was $\approx$0.3°. The apex angles of the prisms (21.38° and 21.72°) were chosen to optimize the precision of the index measurements assuming a nominal index of 2.3.

The refractive indices were measured at 27 wavelengths within the LISe transparency range (from 0.625 to 12 μm) using the conventional technique of minimum deviation angle. A beam from an incandescent lamp or from a globar was forwarded through a SPM2 prism monochromator for wavelength selection. The LISe prisms were positioned on the axis of a G5 goniometer inside a special copper block with an electric heater inside. The temperature was stabilized with an accuracy of 0.5°C in the 20°C–150°C range. A combination of a photomultiplier, a Ge phototransistor, and a cooled HgCdTe detector permitted one to cover the spectral range from the visible to the mid-IR. The beam-shaping optics in our setup contained only reflective elements (systems of cylindrical concave mirrors) in order to minimize the wavelength dependence. The desired polarization was selected using a set of film or grid polarizers. The three refractive indices were measured with an accuracy of $\pm$0.0001 at five temperatures: 293 K (20°C), 323 (50), 353 (80), 393 (120), and 423 K (150°C). From the obtained data, the
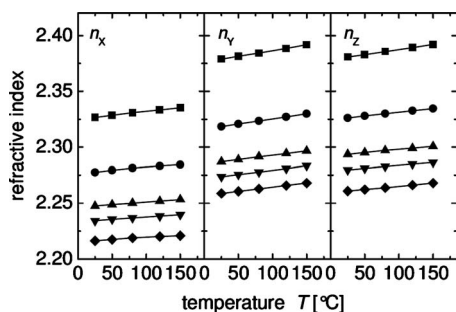

Fig. 5. Refractive indices n_X, n_Y, and n_Z of LISe measured from room temperature to 150°C at 0.8 μm (squares), 1.2 μm (circles), 3 μm (up-triangles), 6 μm (down triangles), and 9 μm (diamonds).

Table 2. Thermo-optic Index Variation dn_i/dT (10^{-5} K^{-1}) of LISe

λ (μm)	dn_X/dT	dn_Y/dT	dn_Z/dT
0.8	6.96	10.79	8.96
1.2	5.44	9.04	6.80
3.0	4.48	7.68	5.68
6.0	4.24	8.00	5.44
9.0	3.76	7.44	5.68

normalized thermo-optic coefficients $\beta=(1/n)dn/dT$, where n is the index of refraction, were calculated.

The temperature dependence of the refractive indices for LISe is plotted in Fig. 5 for different polarization directions and for five wavelengths selected in the transparency range. One can see that the temperature dependence of $n(T)$ is linear at all five wavelengths shown, which means that for all cases the thermo-optic coefficients are almost independent of temperature. That is why $\beta_i(\lambda,T) = a_1(\lambda)$ can be assumed. Dispersion equations based on the last relation will be derived in Subsection 6.B.

At $\lambda \geq 3.0$ μm, where the thermo-optic coefficients of LISe are practically independent of wavelength, their values are 1.5–2 times higher than those of LIS [60,63]. The thermo-optic index variation dn_i/dT for five different wavelengths in the LISe transparency range is given in Table 2. One can see that the thermo-optic effect in LISe is anisotropic: dn_Y/dT is 1.5–2 times higher than dn_X/dT, and dn_Z/dT has intermediate values. While being comparable to AGSe, dn_i/dT for LISe are two to three times smaller than the thermo-optic coefficients of AGS [60,63]. Using the obtained values for the thermal conductivity K and the thermo-optic coefficients β_i one can see that, for given α, l, P, and w_0 values, the thermal lens effect in LISe is about ten times weaker than in AGS.

5. ELECTRICAL PROPERTIES
Three different plates of dimensions 5 mm × 5 mm × 1 mm, greenish in color, were used for the measurements of the electrical properties. Each of them was cut perpendicular to a crystallographic (optical) direction, respectively, along the $a(Y)$, $b(X)$, and $c(Z)$ axes, with the last one being the polar direction. Au electrodes were sputtered on the two opposite major faces. The samples were inserted in a homemade cell always connected to a membrane pump so that no humidity could disturb the experiment. The temperature was controlled using a Pt-resistor directly in thermal contact with the sample. It could be monitored between 80 and 450 K with an accuracy better than 0.1 K using a temperature controller LakeShore 340.

Most of the electrical measurements were performed using a dynamic method under a linear temperature variation (typically 1 or 0.5 K/min, or sometimes—for the pyroelectric coefficient determination—more quickly). Low rates were used in order to avoid temperature gradient within the sample. The direct current (dc) resistivity and the pyroelectric coefficient were deduced by recording the current versus temperature under a constant voltage/

zero bias with a Keithley 236 electrometer. The dielectric response was measured using a HP 4284 impedance analyzer, which can cover a frequency range from 20 Hz to 1 MHz, under a weak alternating current (ac) field ($\sim$0.01 kV/cm).

We did not perform electro-optic experiments on LISe samples. Although in their early measurements Negran *et al.* [13] did not account for the piezoelectric contribution it can be expected from their results that the electro-optic coefficients of LISe are 2.1–2.6 times larger than those of LIS [12].

A. Dielectric Constant

By measuring the sample capacitance and dielectric losses $\tan \delta_\varepsilon = \varepsilon_2/\varepsilon_1$, the dielectric constant $\varepsilon = \varepsilon_1 - j\varepsilon_2$ can be deduced. The LISe permittivity was found to be insensitive to the ac field amplitude and to the dc field strength eventually applied during the experiment. Moreover, no dispersion can be detected in the available frequency range for $T < 350$ K.

Figure 6 displays ε, for the three studied samples at a fixed frequency, as a function of temperature, the only parameter that affects the permittivity value. Within the experimental errors (about 5%, especially due to the electrode area determination), $\varepsilon_X = \varepsilon_Y = 20.7 \pm 1$ at room temperature ($T = 300$ K), whereas ε_Z is slightly lower (19.1 ± 1). When increasing the temperature from 80 to 450 K, ε increases for the three directions nearly in a linear way at least up to 350 K as shown in Fig. 6 ($\varepsilon_i = \varepsilon_{i0} + \alpha_{\varepsilon i} T$, where $i = X$, Y, or Z). No anomaly, like a peak or a shoulder, which may be associated with a phase transition or a relaxation process, can be observed. The $\alpha_{\varepsilon X}$ and $\alpha_{\varepsilon Y}$ coefficients are almost equal, about $(4.1 \pm 0.1) \times 10^{-3}$ K^{-1}, and $\alpha_{\varepsilon Z}$ is slightly higher, $(4.6 \pm 0.1) \times 10^{-3}$ K^{-1}. At higher temperature ($T > 350$ K), ε increases more rapidly, especially in the X direction; the deviation from the linear dependence observed at low temperatures increases for lower measuring frequencies. This is an indication that a conductivity term contributes to the measured dielectric constant for $T > 350$ K.

B. Electric Conductivity

The dielectric losses are lower than 0.001 up to 350 K (Fig. 7) but increase strongly for higher temperatures. They increase also when the measuring frequency decreases. For example, in the X direction (see Fig. 7), $\tan \delta_\varepsilon$

Fig. 7. Dielectric losses measured along the directions X (10, 30, and 100 kHz), Y (100 kHz), and Z (100 kHz) (left scale), together with the ac conductivity (right scale) measured in the X direction at 10, 30, and 100 kHz and plotted as a function of $1/T$.

varies, at 450 K, from 7% at 100 kHz up to 53% at 10 kHz. The values measured along the Y and Z axes are nearly the same (about 1.7% at 450 K and 100 kHz) but much lower than along the X-axis, reflecting an anisotropic conductivity ($\sigma_X > \sigma_Y, \sigma_Z$). The ac conductivity can be defined as $\sigma_{ac} = \varepsilon_0 \varepsilon_2 \omega$ (ε_0 is the vacuum permittivity). The curve σ_{ac} versus $1/T$ in a semi-logarithmic scale (Fig. 7) displays a straight line, which means that the ac conductivity follows an Arrhenius law.

The fitted activation energy, in the X direction, is $E_a = 0.74$ eV. Moreover, no variation with frequency can be detected between 350 and 450 K. Usually, σ_{ac} is considered to be the sum of two terms: $\sigma_{ac} = \sigma_{dc} + A_\sigma \omega^n$, where the former term is the dc conductivity and comes from entities capable to travel all over the sample and the second one, which induces a frequency dependence, is due to ions jumping between equivalent crystallographic sites. One may thus conclude that the LISe conductivity comes mainly from the dc term. It was directly determined by measuring the dc current under a weak dc bias (0.1 kV/cm). The thermal variation of the dc resistivity
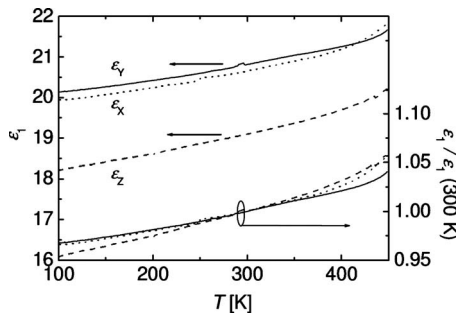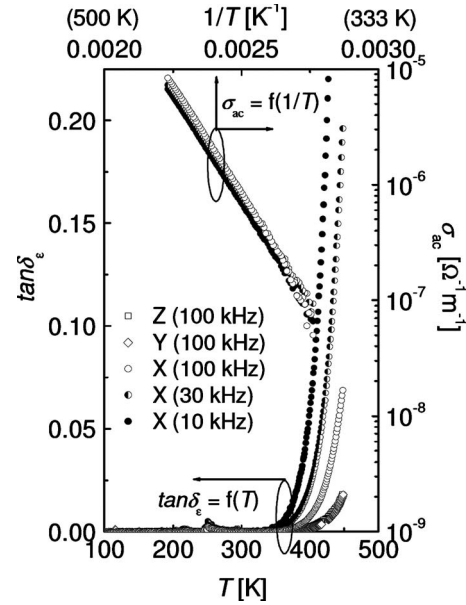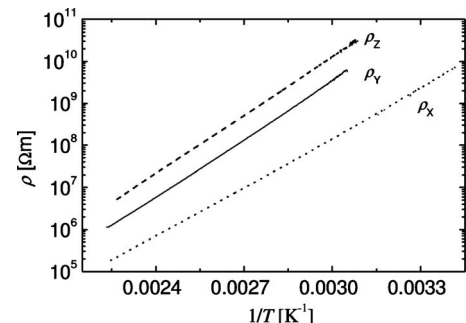

Fig. 6. Real part of the dielectric permittivity measured at 100 kHz along the X (dotted line), Y (solid line), and Z (dashed line) directions (left scale) and normalized dielectric constant [defined as $\varepsilon_1/\varepsilon_1 (300$ K)] exhibiting a nearly linear variation up to 350 K (right scale).

Fig. 8. Measured dc resistivity ρ as a function of $1/T$ under 0.1 kV/cm along X (dotted line), Y (solid line), and Z (dashed line).

($\rho = 1/\sigma_{dc}$) is reported in Fig. 8. Clearly ρ is associated with an activated and anisotropic process.

The electric conductivity is about ten times higher along the X-axis than along Y or Z. The deduced activation energy changes also with the crystal orientation. For the Y and Z directions, $E_a = 0.92$ eV, and for the X direction, $E_a = 0.77$ eV, in accordance with the previous determination from the dielectric measurements. These values are much lower than half of the direct bandgap (see Section 3) but agree with the indirect or pseudo-direct fundamental bandgap determined at the onset of optical absorption (2.03 eV at 300 K [33]).

C. Pyroelectric Coefficients

The determination of the pyroelectric coefficients p was performed by measuring a current under constant thermal variation: $|i(T)| = S p |dT/dt|$ (S is the electrode area). We first checked that no current can be detected for the samples cut perpendicularly to the X or Y direction, and that both reversing the crystal orientation (i.e., $Z \equiv c$-axis up or down) and cooling instead of heating indeed change the sign of the recorded current. Moreover, as expected, $i(T)$ (about 0.4–0.8 pA for +1 K/min) was found to be proportional to the heating rate. These observations allow one to ascribe $i(T)$ to the variation of the spontaneous polarization and thus to determine the pyroelectric coefficient between 100 and 350 K. For higher temperatures, diffusion of some charged species occurs and screens the pyroelectricity. The p coefficient is a linear increasing function of the temperature, following (Fig. 9)

$$p(T) = 1.5 \times 10^{-10} + 4.72 \times 10^{-12} T. \tag{6}$$

The extrapolated value at 300 K, with a maximum error bar within 10%, is $(1.6 \pm 0.2) \times 10^{-9}$ C K^{-1} cm^{-2}, more than twice the value obtained in the same way for LIS $(0.6 \times 10^{-9}$ C K^{-1} cm^{-2} [65]). This ratio is very close to the early result of Negran *et al.* [13] although their absolute values are 2.3–2.5 times lower. Like in the previous studies, our attempt to reverse the polarization by applying a strong dc field (up to 10 kV/cm) failed and the ferroelectric nature of the room temperature phase of LISe has not been evidenced. However, the present study extends the investigation of the dielectric permittivity of LISe to a wider frequency range and higher temperatures. It reveals both a conductivity contribution and an anisotropic behavior and confirms the linear change of the permittivity with the temperature ($T < 350$ K). The conductivity is
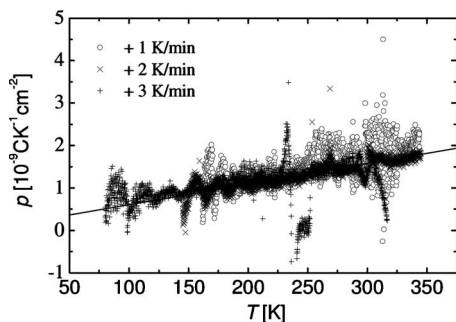

Fig. 9. Pyroelectric coefficient p as a function of the temperature T determined for three different heating rates. The solid line represents the linear variation of its thermal dependence.

known to be very sensitive to the sample stoichiometry [46], especially to the Li and Se vacancies. The high resistivity of our samples ($>3 \times 10^{11}$ Ω cm), whatever is their orientation, and the fact that an Arrhenius law describes the $\rho(T)$ behavior down to room temperature (i.e., without a cusp indicating a change to an extrinsic regime [46]) are both evidence for the good chemical quality of the investigated samples.

6. LINEAR OPTICAL AND THERMO-OPTIC DISPERSIONS

The linear optical and thermo-optic dispersion relations allow one to predict accurately the phase-matching directions and temperature tunability which is most important for a nonlinear optical material. The initial work of Negran *et al.* [13] contained only refractive index measurements at 633 nm. Similar to LIS [12], LISe is negative biaxial with the correspondence $XYZ \equiv bac$, and the two refractive indices n_Y and n_Z are very close. Our initial index measurements in the 0.5–11 μm range with yellow color LISe were tabulated in [29] where the first one-pole Sellmeier equations with quadratic IR-terms were constructed. Additional refractive index measurements between 0.7 and 1.9 μm of yellow-greenish (as grown) and dark red (annealed) LISe indicated that the index of refraction is the same within the experimental error [27]. Another similar fit for the 0.5–10 μm spectral range appeared in [51,66] but its origin is unknown. An alternative measurement of the refractive indices of red color LISe from 0.633 to 10 μm was published in [19], together with two-pole Sellmeier equations, which were also reproduced elsewhere [52], and another index measurement with deep red LISe was used to create a further Sellmeier set specified for the 0.5–12 μm spectral range and based again on two poles [20,21] (see also [67,68]), but it is unclear if a refinement with second-harmonic generation (SHG) experimental angles in the 9.2–9.6 μm spectral range (X-Z plane) was used for its derivation.

A. Sellmeier Equations at Room Temperature

Having in mind the different predictions of all the available sets of Sellmeier equations we decided to remeasure first the index of refraction of high crystal quality yellow LISe using the technique of minimum angle deviation. The room temperature results in the 0.525–12 μm spectral range are included in Table 3.

Then, imposing that the IR poles match the In–Se phonon wavelengths [57], a starting (raw) set of Sellmeier equations was derived. The further refinement was based on narrowband CW difference-frequency generation (DFG) phase-matching data in the 5.9–8.1 μm range (a LISe sample of greenish color cut at $\varphi = 55°$ in the X-Y plane was used for these measurements; see Subsection 9.A), the signal wavelength (1537 nm) obtained at normal incidence in the optical parametric oscillator (OPO) experiment with 1064 nm pumping ($\varphi = 72°$ crystal cut in the X-Y plane with a yellow color sample) [69], a SHG value of $\varphi = 70.39°$ in the X-Y plane measured at 2.845 μm with femtosecond pulses and yellow LISe [29], and SHG angles measured in the X-Z plane ($\theta = 17.62°$ at 2.23 μm, with femtosecond pulses and yellow LISe [29] and $\theta = 30°$

Table 3. New Data on the Refractive Indices of LISe at 25°C

λ (μm)	n_x	n_y	n_z
0.525	2.4808	2.5551	2.5554
0.55	2.4513	2.5197	2.5216
0.6	2.4081	2.4718	2.4723
0.65	2.3787	2.4371	2.4388
0.7	2.3567	2.4126	2.4143
0.75	2.3399	2.3937	2.3954
0.8	2.3266	2.3789	2.3807
0.84	2.3193	2.3663	2.371 42
0.89	2.3113	2.3566	2.3623
0.94	2.3038	2.3484	2.3543
1	2.297 23	2.341	2.3477
1.1	2.2876	2.3299	2.3372
1.25	2.2776	2.3185	2.3261
1.45	2.268 14	2.3091	2.315 33
1.65	2.2608	2.302 61	2.3079
1.8	2.2578	2.298 67	2.3048
2	2.2557	2.2961	2.3022
3	2.2477	2.287	2.2937
4	2.2427	2.2822	2.2883
5	2.2388	2.2775	2.2841
6	2.2343	2.2736	2.2796
7	2.2295	2.2689	2.2742
8	2.2231	2.264	2.2683
9	2.2163	2.2587	2.2609
10	2.2084	2.2511	2.2537
11	2.199	2.2414	2.2435
12	2.1879	2.2315	2.2332

measured at 9.55 μm with nanosecond pulses and red LISe [52]). The SHG values were essential to tighten the fits obtained. The final result for the Sellmeier equations is

$$n_x^2(\lambda) = 5.669\ 848 + \frac{0.194\ 852\ 5}{\lambda^2 - 0.094\ 737\ 86} + \frac{300.727\ 08}{\lambda^2 - 492.0924},$$

$$n_y^2(\lambda) = 5.676\ 208 + \frac{0.245\ 157\ 9}{\lambda^2 - 0.062\ 651\ 55} + \frac{205.055\ 97}{\lambda^2 - 432.8862},$$

$$n_z^2(\lambda) = 6.302\ 234 + \frac{0.250\ 905\ 2}{\lambda^2 - 0.041\ 374\ 38} + \frac{755.686\ 22}{\lambda^2 - 713.0767}.$$

$$(7)$$

The above set of Sellmeier equations predicts no anomalous index crossing at shorter wavelengths down to the transparency edge of LISe, in contrast with the predictions of the equations derived in [19,51,52,66]. This means that the two optic axes which determine the directions where the index of refraction is independent of polarization remain in the *X-Z* principal plane for the whole transparency range. The angle V_Z between them and the *Z*-principal optical axis, determined from $\sin V_Z = n_Z(n_Y^2 - n_X^2)^{1/2}/n_Y(n_Z^2 - n_X^2)^{1/2}$, is shown in Fig. 10. Its wavelength dependence is stronger near the transparency edges but
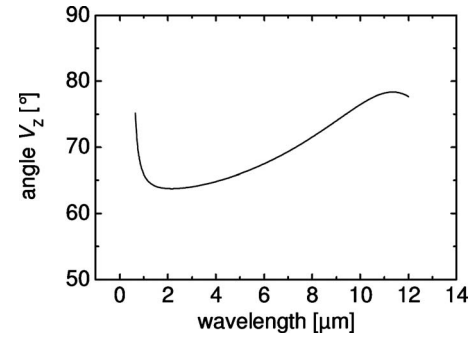

Fig. 10.   Angle V_Z between the optic axes and the principal *Z*-axis of LISe calculated by the new Sellmeier equations derived in the present work.

this angle remains between 63° and 79° in the whole transparency range which means that LISe is a negative biaxial crystal. It can be also regarded as quasi-uniaxial, which is a consequence of the fact that the two indices n_Y and n_Z are very close. Therefore no phase-matching can be expected for propagation directions in the vicinity of the *X*-principal axis.

The experimental DFG angles in the 6.23–6.81 μm range, obtained at normal incidence (see Table 4), and the OPO and SHG angles are reproduced with an accuracy of ±0.6° with this set of equations. A comparison with the other four available Sellmeier equations and the experimental data for SHG in the *X-Y* and *X-Z* principal planes is given in Fig. 11. In the *X-Y* plane the predictions of the new Sellmeier equations are closest to [20,21,29] at short wavelengths and to [19] at longer wavelengths. In the *X-Z* plane substantial differences are observed at longer fundamental wavelengths with strongest deviation from the predictions of [19,29].

B. Thermo-optic Dispersion Relations
A similar fitting procedure as for LIS [12] was used to obtain expressions for the wavelength dependence of the normalized thermo-optic coefficients of LISe, but in this case a first-order approximation in temperature was sufficient, and $\beta_i(\lambda, T) = a_1(\lambda)$ (see Subsection 4.D) is fitted to

Table 4. DFG Phase-Matching Data Obtained with LISe in the *X-Y* Plane

| λ_3 (μm)	λ_2 (μm)	φ_{exp} (deg)	φ_{calc} (deg)
0.775 452 3	0.885 653 3	55	54.4285
0.771 045 7	0.878 958 6	55	54.4031
0.766 477 3	0.872 379 6	55	54.4969
0.761 290 0	0.864 790 1	55	54.5524
0.755 543 8	0.856 274 4	55	54.5623
0.750 395 8	0.848 997 4	55	54.6954
0.745 456 5	0.841 821 7	55	54.7408
0.740 477 4	0.834 724 5	55	54.8325
0.735 667 3	0.827 814 6	55	54.8919
0.730 866 0	0.821 018 0	55	54.9864
0.726 121 5	0.814 325 6	55	55.0833
0.721 516 3	0.807 767 5	55	55.1435
0.716 881 9	0.801 288 5	55	55.2516
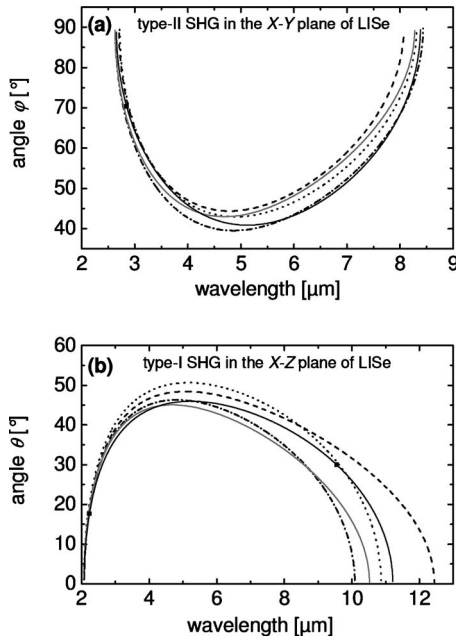
Fig. 11. Calculated SHG phase-matching angles in the (a) *X-Y* and (b) *X-Z* principal planes of LISe using the refined Sellmeier equations from the present work (solid lines) and older Sellmeier equations: [19], dashed-dotted lines; [20,21], dotted lines; [51,66], gray lines; and [29], dashed lines. The symbols correspond to experimental data (see text).

the following two-pole functional form using the measurements performed for all 27 wavelengths in the main part of the LISe transparency range:

$$a_1(\lambda) = A_1 + \frac{A_3}{\lambda^2 - A_2} + \frac{A_5}{\lambda^2 - A_4}. \tag{8}$$

The five fitting parameters are compiled in Table 5. The obtained fitting curves together with the experimental results for the three polarizations are shown in Fig. 12.

On the basis of the data obtained the temperature dependence of the phase-matching can be analyzed. According to the definition of β_i the index of refraction at a given temperature T will be given by

$$\frac{n(\lambda, T)}{n(\lambda, T_0)} = \exp[a_1(\lambda)(T - T_0)] \approx 1 + a_1(\lambda)(T - T_0), \tag{9}$$

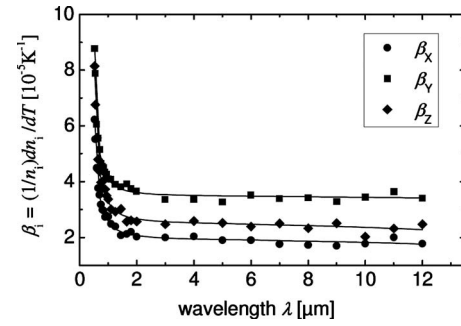where $T_0 = 25\,^\circ\text{C}$ and $n(\lambda, T_0)$ is given by Eqs. (7).

Fig. 12. Normalized thermo-optic coefficients measured in the transparency range of LISe along the three principal optical axes: experimental points (symbols) and fits (curves).

7. PHASE-MATCHING INVESTIGATIONS

A. Effective Nonlinearity and Hobden Classification

The phase-matching loci and the effective nonlinearity for LISe will be analyzed in the *XYZ*-principal optic axis frame, but the tensor elements of the nonlinear susceptibility are defined traditionally, in accordance with ANSI/IEEE Std 176-1987 [70], in the *abc*-crystallographic frame, where c is the polar twofold axis. The chosen convention $n_X < n_Y < n_Z$ in order to have the two optic axes in the *X-Z* principal plane affects therefore the expressions for the effective second-order nonlinearity d_{eff}. The general form of the contracted d-tensor for the orthorhombic class $mm2$ reads

$$
\begin{bmatrix}
0 & 0 & 0 & 0 & d_{15} & 0 \\
0 & 0 & 0 & d_{24} & 0 & 0 \\
d_{31} & d_{32} & d_{33} & 0 & 0 & 0
\end{bmatrix}. \tag{10}
$$

For an arbitrary propagation direction assuming collinear interaction and neglecting the spatial walkoff effect analytical expressions for d_{eff} can be derived in our conventions from the general formulas presented by [71]

$$
\begin{aligned}
d_{\text{eff}}^{ss-f} = {} & 2d_{15} \sin\theta \cos\delta(\cos\theta \sin\varphi \sin\delta - \cos\varphi \cos\delta) \\
& \times (\cos\theta \sin\varphi \cos\delta + \cos\varphi \sin\delta) \\
& + 2d_{24} \sin\theta \cos\delta(\cos\theta \cos\varphi \cos\delta - \sin\varphi \sin\delta) \\
& \times (\cos\theta \cos\varphi \sin\delta + \sin\varphi \cos\delta) \\
& + d_{31} \sin\theta \sin\delta(\cos\theta \sin\varphi \cos\delta + \cos\varphi \sin\delta)^2 \\
& + d_{32} \sin\theta \sin\delta(\cos\theta \cos\varphi \cos\delta - \sin\varphi \sin\delta)^2 \\
& + d_{33} \sin^3\theta \cos^2\delta \sin\delta, \tag{11}
\end{aligned}
$$

Table 5. Fitting Parameters Describing the Thermal and Wavelength Dispersion of the Principal Thermo-optic Coefficients $\beta_i(\lambda, T) = a_1(\lambda)$ of LISe. The i-Label Denotes the Polarization Direction ($i = X, Y, Z$).

i	A_1 $(10^{-5}\,^\circ\text{C}^{-1})$	A_3 $(10^{-6}\,^\circ\text{C}^{-1}\,\mu\text{m}^2)$	A_5 $(^\circ\text{C}^{-1}\,\mu\text{m}^2)$	A_2 (μm^2)	A_4 (μm^2)
X	2.783 71	5.4189	0.007 32	0.149 498	855.280
Y	4.262 16	4.9903	0.013 97	0.182 457	1791.66
Z	3.587 43	6.2562	0.008 73	0.161 387	807.974

$$
\begin{aligned}
d_{\text{eff}}^{fs\text{-}f} = d_{\text{eff}}^{sf\text{-}f} = &-d_{15}[\ \sin\theta\cos\delta(\cos\theta\sin\varphi\sin\delta \\
&-\cos\varphi\cos\delta)^2 + \sin\theta\sin\delta(\cos\theta\sin\varphi\sin\delta \\
&-\cos\varphi\cos\delta)(\cos\theta\sin\varphi\cos\delta+\cos\varphi\sin\delta)] \\
&-d_{24}[\sin\theta\cos\delta(\cos\theta\cos\varphi\sin\delta+\sin\varphi\cos\delta)^2 \\
&+\sin\theta\sin\delta(\cos\theta\cos\varphi\cos\delta-\sin\varphi\sin\delta) \\
&\times(\cos\theta\cos\varphi\sin\delta+\sin\varphi\cos\delta)] \\
&-d_{31}\sin\theta\sin\delta(\cos\theta\sin\varphi\sin\delta-\cos\varphi\cos\delta) \\
&\times(\cos\theta\sin\varphi\cos\delta+\cos\varphi\sin\delta) \\
&-d_{32}\sin\theta\sin\delta(\cos\theta\cos\varphi\cos\delta-\sin\varphi\sin\delta) \\
&\times(\cos\theta\cos\varphi\sin\delta+\sin\varphi\cos\delta) \\
&-d_{33}\sin^3\theta\sin^2\delta\cos\delta,
\end{aligned} \tag{12}
$$

for type-I and type-II phase-matching, respectively, where the superscripts "s" and "f" stand for the "slow" and "fast" eigenmodes and their sequence follows the usual convention $\lambda_1\lambda_2\lambda_3$ with $\lambda_1 > \lambda_2 > \lambda_3$. The angle δ whose introduction simplifies the expressions and which is determined from

$$
\begin{aligned}
\tan 2\delta = \cos\theta\sin 2\varphi[\cot^2 V_Z\sin^2\theta+\sin^2\varphi \\
-\cos^2\theta\cos^2\varphi]^{-1} \quad (0<2\delta<\pi)
\end{aligned} \tag{13}
$$

defines the polarization directions of the slow and fast waves which are orthogonal to each other. It is the angle between the polarization direction of the slow wave and the plane of propagation containing the principal Z-axis.

In the principal planes the expressions for d_{eff} [Eqs. (11) and (12)] are reduced to

$$
d_{\text{eff}}^{eoe} = d_{\text{eff}}^{oee} = -(d_{24}\sin^2\varphi+d_{15}\cos^2\varphi) \quad (X\text{-}Y\ \text{plane}),
\tag{14}
$$

$$
d_{\text{eff}}^{oeo} = d_{\text{eff}}^{eoo} = -d_{24}\sin\theta \quad (Y\text{-}Z\ \text{plane}), \tag{15}
$$

$$
d_{\text{eff}}^{ooe} = d_{31}\sin\theta \quad (X\text{-}Z\ \text{plane},\ \theta<V_Z), \tag{16}
$$

$$
d_{\text{eff}}^{eoe} = d_{\text{eff}}^{eoo} = -d_{15}\sin\theta \quad (X\text{-}Z\ \text{plane},\ \theta>V_Z), \tag{17}
$$

with superscripts "o" and "e" denoting the ordinary and extraordinary beams. LISe behaves as an optically negative uniaxial crystal in the X-Y and X-Z (for $\theta<V_Z$) planes and as an optically positive uniaxial crystal in the Y-Z and X-Z (for $\theta>V_Z$) planes. Assuming the Kleinman symmetry condition to hold then $d_{15}=d_{31}$ and $d_{24}=d_{32}$.

The biaxial phase-matching loci for collinear SHG can be categorized using the classification of Hobden [72]. Our calculations based on the relatively simple transcendental equations derived in [73] predict that no phase-matched SHG is possible below 1860 nm. LISe enters Hobden's class 13 at 1860 nm, class 11 at 2078 nm, class 10 at 2672 nm, and class 9 at 3051 nm; then it goes back to class 10 at 7799 nm, to class 11 at 8259 nm, to class 13 at 10881 nm; and finally no SHG phase-matching is possible again above 11071 nm. These transitional fundamental wavelengths correspond to propagation directions along the Y- or along the Z-principal axes [noncritical

phase-matching (NCPM)] either for the *ss-f* or the *fs-f* ($\equiv sf$-f) polarization configurations.

Figure 13 illustrates the different classes for SHG in LISe at several representative fundamental wavelengths. The surface of the unit sphere is projected onto the X-Z plane of the crystal. The direction of the wave vectors of the interacting waves for phase-matching as given by their interception with the surface of the unit sphere is plotted. The stereographic projection of the first octant is presented only but the loci in the other octants can be obtained by mirror reflections across the principal planes.

We do not present plots of the angle δ which can be easily calculated from Eq. (13). Its dispersive properties (determined by the angle V_Z) lead to slightly different values at the three interacting wavelengths but normally the effect of this on the conversion efficiency can be neglected. Qualitative arguments relating the spatial walk-off (magnitude and direction) to the topology depicted in Fig. 13 can be found in [74]. The calculation of the spatial walk-off for an arbitrary propagation direction is beyond the scope of this paper but several works provide suitable approaches to this aim [75–78]. Analytical approaches for the estimation of acceptance parameters based on the small-signal approximation in the general case of biaxial crystals can be found in [76,77]. We note here only that since the angle V_Z for LISe in the major part of the transparency range (Fig. 10) is not far from 90°, the dispersive properties and in particular the spectral acceptance are
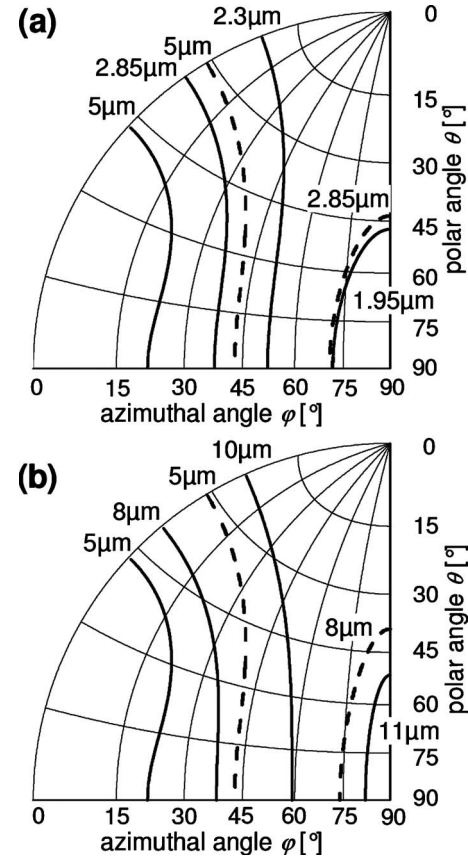

Fig. 13. Stereographic projections of the SHG in the first octant of LISe calculated for wavelengths representative of the Hobden classes. Type-I (*ss-f*) interaction (solid lines) and type-II (*fs-f* $\equiv sf$-f) interaction (dashed lines).

not expected to be substantially modified by propagation outside the principal planes. Figure 13 indicates that double solutions for the angles exist (e.g., for Hobden's class 9) which is equivalent to the existence of points outside the principal planes where $\partial\varphi/\partial\theta=0$ holds. This means that NCPM in one direction can also occur outside the principal planes (e.g., at $\varphi\approx23.2°$, $\theta\approx70.3°$ for *ss-f* type SHG at 5 μm).

B. SHG in Principal Planes

The SHG phase-matching directions in the principal planes are shown in the lower part of Fig. 14. The first and third panels (*X-Y*) and (*X-Z*) in the bottom part correspond to the plots in Figs. 11(a) and 11(b), respectively. The transitional wavelengths enumerated above can be easily identified there. The SHG ranges where $d_{\mathrm{eff}}\neq0$ are 2078–10881 nm for type-I (*oo-e*) phase-matching in the *X-Z* plane, 2672–8259 nm for type-II (*eo-e*) phase-matching in the *X-Y* plane, and 2672–3051 and 7799–8259 nm for type-II (*oe-o*) phase-matching in the *Y-Z* plane. We observe an interesting feature in this crystal: the SHG limits with $d_{\mathrm{eff}}\neq0$ are larger for propagation outside the principal planes where type-I phase-matching down to 1860 nm and up to 11071 nm is possible. Under the convention $n_X<n_Y<n_Z$ the largest birefringence and consequently the shortest SHG wavelength are obviously achieved for type-I interaction and propagation along the *Y*-axis. However, in LISe (similarly to LIS [12]) when the *Y*-axis is approached in the principal planes *X-Y* or *Y-Z*, d_{eff} for type-I interaction vanishes and this is true also for the limiting case of propagation along the *Y*-axis. This is the reason why propagation outside the principal planes can be used, e.g., to shorten the SHG lower wavelength limit (Fig. 13). A similar situation has been observed previously in KT:OPO$_4$ (KTP) [79].

It is seen from Fig. 14 that in the *Y-Z* plane the type-II interaction is quasi-angle-noncritical which ensures a large acceptance angle and a small walkoff angle (compare Fig. 15). In contrast, type-I interaction in the *X-Z*
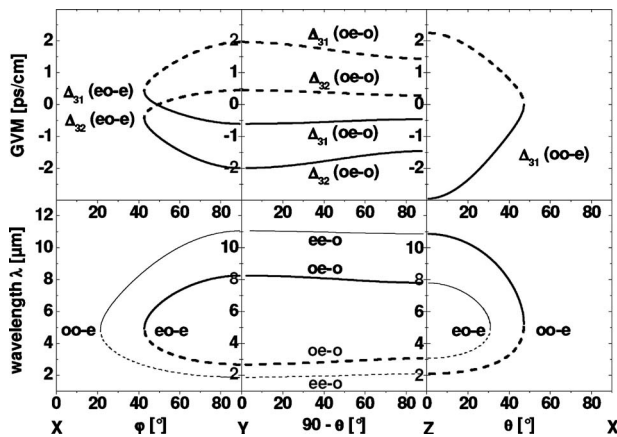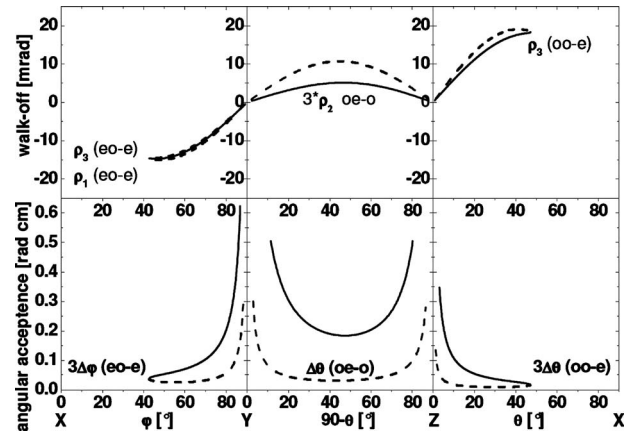

Fig. 15.   SHG internal angular acceptance (bottom) and walkoff angles (top) in the principal planes of LISe. Thick solid lines correspond to the branches with longer wavelengths from Fig. 14 and thick dashed lines correspond to the branches with shorter wavelengths. Only the cases with $d_{\mathrm{eff}}\neq0$ are included.

plane and type-II interaction in the *X-Y* plane have regions of quasi-wavelength-NCPM ($\partial\Phi/\partial\lambda\approx0$) centered at 5223 and 4919 nm, respectively (Fig. 14). Letting $\Phi=\varphi$ or θ, the walkoff angles in the upper panels of Fig. 15 are calculated using the simplified formula $\rho_i=[n_i^e(\Phi)]^{-1}\partial n_i^e/\partial\Phi$ valid for uniaxial crystals, where the subscript $i=1,2,3$ is associated with wavelengths λ_i ($\lambda_3^{-1}=\lambda_1^{-1}+\lambda_2^{-1}$) and $n_i^e(\Phi)$ is the extraordinary index of refraction of the walking-off wave as given by the uniaxial analogy in the principal planes. We preserved its sign which is in accordance with the corresponding phase-matching angles, i.e., a positive value of the walk-off means that the Poynting vector is at an angle larger than the phase-matching angle, and vice versa. Note that the walk-off is very similar for the two branches of the solution for phase-matching in all three principal planes. In the *X-Y* plane these branches and the two different walkoff parameters (we have here two extraordinary waves) are almost undistinguishable. The maximum walk-off amounts to $\rho_3=1.09°$ in the *X-Z* plane for SHG at ~3.39 μm.

The acceptance angle is evaluated from the phase velocity mismatch $\Delta\kappa(\delta\Phi)$ due to an angular deviation $\delta\Phi=\Phi-\Phi_{\mathrm{PM}}$ of the wave vectors around the nominal phase-matched direction Φ_{PM}. A Taylor expansion of $\Delta\kappa$ leads to

$$\Delta\kappa(\delta\Phi)=\gamma_{\mathrm{CPM}}\delta\Phi+\gamma_{\mathrm{NCPM}}(\delta\Phi)^2+\cdots,\qquad(18)$$

where $\gamma_{\mathrm{CPM}}=[\partial(\Delta k)/\partial\Phi]_{\Phi=\Phi_{\mathrm{PM}}}$ vanishes for NCPM (i.e., for $\Phi=0,90°$) and $\gamma_{\mathrm{NCPM}}=(1/2)[\partial^2(\Delta k)/\partial\Phi^2]_{\Phi=\Phi_{\mathrm{PM}}}$. The acceptance angle, defined as the bandwidth at full width at half-maximum (FWHM) of the sinc$^2(\Delta kl/2)$ phase-match function, is given by $\Delta\Phi=2.784/|\gamma_{\mathrm{CPM}}|l$ for critical phase-matching, while for NCPM it is $\Delta\Phi=|2.784/\gamma_{\mathrm{NCPM}}l|^{1/2}$. The lower panels of Fig. 15 display the acceptance angles (for a length $l=1$ cm) in the three principal planes. The acceptance curves, computed with only γ_{CPM} in expansion (18), are interrupted near noncriticality at maximum values corresponding to the ones calculated for $l=1$ cm using γ_{NCPM} only. Although that type of presentation in Fig. 15 is not very accurate in these limits it permits the results to be presented as scalable with respect to the crystal

Fig. 14.   SHG phase-matching in the principal planes of LISe. Thick lines in the lower part show fundamental wavelengths for which $d_{\mathrm{eff}}\neq0$ and thin lines indicate cases where d_{eff} vanishes. The inverse group velocity mismatch (GVM) ($\Delta_{31}=1/v_3-1/v_1$ and $\Delta_{32}=1/v_3-1/v_2$, where v_1, v_2, and v_3 denote the group velocities at λ_1, λ_2, and λ_3) is shown in the upper part only for the cases where $d_{\mathrm{eff}}\neq0$. The solid (dashed) lines correspond to the branch with longer (shorter) wavelengths.

length l (simultaneous consideration of both derivatives would not allow this).

The chosen presentation of the inverse group velocity mismatch in Fig. 14 is equivalent to the spectral acceptance $\Delta\nu$ but contains the sign as additional information. In the simplest cases of type-I SHG or degenerate DFG we have, e.g., $\Delta\nu l = 0.886/|\Delta_{31}|$, and the gain bandwidth in optical parametric amplification assuming a narrowband pump wave at λ_3 is inversely proportional to $|\Delta_{21}| = |1/v_2 - 1/v_1|$. The two parameters Δ_{31} and Δ_{32} vanish at 5223 nm in the *X-Z* plane which means large spectral acceptance for SHG of short pulses where the second derivative of the wave vector mismatch comes into play [20,21]. The situation is different for type-II interaction in the *X-Y* plane: here $\Delta_{32} = -\Delta_{31}$ at 4919 nm, at 3701 nm Δ_{32} vanishes, and at 6328 nm Δ_{31} vanishes, but in none of these cases an extremum of the spectral acceptance occurs because in type-II SHG of short pulses all three waves should be considered as broad band.

C. Sum- and Difference-Frequency Mixing

Type-I phase-matching in the *X-Z* plane for non-degenerate three-wave interactions (sum- and difference-frequency mixing as well as optical parametric generation, amplification, and oscillation) is presented in Fig. 16(a) where two branches of the solution can be seen. The whole transparency range of LISe can be covered for $0° \le \theta \le 40°$ in the *X-Z* plane but d_{eff} increases with the

phase-matching angle θ. Note that $d_{\text{eff}} = 0$ in the noncritical ($\theta = 0°$) configuration and that the situation $\theta > V_Z$ [see Eq. (15)] is never reached. At larger angles θ we observe a retracing behavior in the left branch, e.g., in the case of the OPO one and the same pump wavelength λ_3 corresponds to two pairs (λ_1, λ_2) of signal and idler wavelengths. In this region the spectral acceptance is very large. Thus for $\theta = 45°$ [Fig. 16(a)], $\lambda_1 \approx 9.64~\mu\text{m}$, $\lambda_2 \approx 1.94~\mu\text{m}$, and $\lambda_3 \approx 1.615~\mu\text{m}$ all three group velocities are very close: at this point the absolute values of all the GVM parameters do not exceed 20 fs/mm. This means that this phase-matching configuration is especially suitable for frequency conversion of femtosecond pulses. In optical parametric amplifiers (OPAs) and OPOs this advantage can be utilized, however, only in combination with seeding for control of the spectral bandwidth.

In the regions near the degeneracy points (SHG points) we have on the other hand $\Delta_{21} \approx 0$, but the wave at λ_3 can have in general a different group velocity. Such a regime is attractive for broadband parametric amplification in the field of a narrowband pump pulse as in the case of chirped pulse optical parametric amplification. Increasing the phase-matching angle (curve for $\theta = 45°$ in Fig. 16) the two branches merge into a closed contour and we approach the point where SHG phase-matching only for a single wavelength is possible (see Fig. 14) and all three group velocities are again very close, but the tunability in that case is very limited.

The curves for type-II phase-matching [Fig. 16(b)] have a completely different shape. The two branches of the solution are represented by curves of opposite curvatures which can cross at two points where phase-matching for degenerate DFG or SHG is realized. With decreasing phase-matching angle these branches separate and a single crossing point is reached [between $\varphi = 50°$ and $40°$ in Fig. 16(b)] which corresponds to the single SHG solution in Fig. 14. For yet smaller angles no crossing occurs and the degeneracy point is not reached.

For all phase-matching angles presented we observe again a retracing behavior at longer λ_3: for each λ_3 two couples (λ_1, λ_2) are phase-matched. At the point where these two pairs merge into one (at the maximum λ_3 permitting phase-matching) the waves at λ_1 and λ_2 have equal group velocities and similarly to the case discussed for Fig. 16(a) broadband parametric amplification in the field of a narrowband pump wave can be realized. The deviation from the pump group velocity remains, however, essential. Thus, e.g., at $\varphi = 90°$ and $\lambda_3 = 4330$ nm, $\Delta_{21} \approx 0$ and $\Delta_{31} \approx \Delta_{32} \approx -1.57$ ps/cm. Improved group-matching at this point with the pump wave at λ_3 occurs when decreasing the phase-matching angle φ in accordance with Fig. 14.

Comparing Fig. 16(b) to Fig. 16(a) we note that at relatively short λ_3 (e.g., 1064 nm) full tunability with a fixed crystal cut is achievable only in the *X-Z* principal plane. The group velocity mismatch depends on the specific wavelengths chosen. At $\lambda_3 = 1064$ nm (a case interesting for parametric downconversion) $\Delta_{21}(X\text{-}Z) < \Delta_{21}(X\text{-}Y)$ is fulfilled in the whole transparency range of LISe. This means that type-II phase-matching in the *X-Y* plane is more advantageous for development of narrowband parametric generators or oscillators.
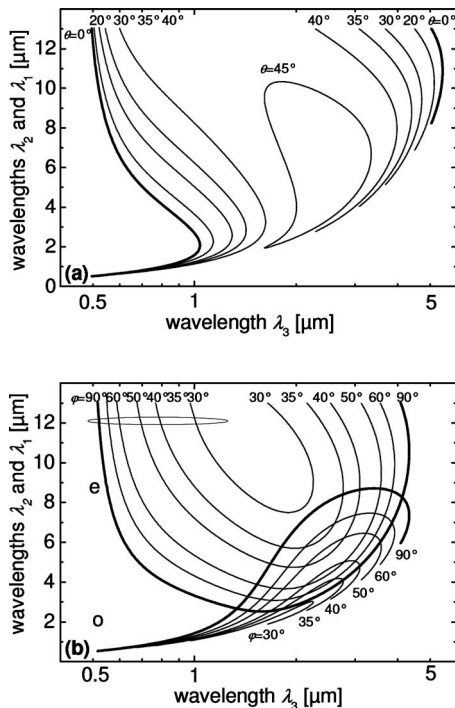
Fig. 16. (a) Type-I (*oo-e*) phase-matching for sum-frequency generation and DFG in the *X-Z* plane of LISe and several values of the polar angle θ: 0°-noncritical configuration, 20°, 30°, 35°, 40°, and 45°. The curves are terminated at the left and top sides by the transparency range of the crystal. (b) Type-II (*eo-e* and *oe-e*) phase-matching for sum-frequency generation and DFG in the *X-Y* plane of LISe and several values of the azimuthal angle φ: 90°-noncritical configuration, 60°, 50°, 40°, 35°, and 30°. The curves are terminated at the left and top sides by the transparency range of the crystal.

Our analysis of the phase-matching properties of LISe is just a first-order approximation because it was based on the small-signal limit where saturation is neglected. We considered also only collinear interaction. Noncollinear interaction attracts recently great interest because in addition to the possibility to improve the tunability, to spatially separate the beams, and to compensate for the spatial walk-off, it can considerably reduce the group velocity mismatch [80]. The latter is very promising for short pulse interactions. Explicit expressions for noncollinear phase-matching in the principal planes of a biaxial crystal can be found in [81] and calculations of noncollinear group velocity matching for arbitrary wave vector directions in [82,83]. Some phase-matching properties of the mixed compounds $LiIn(S_{1-x}Se_x)_2$ were calculated in [20,21,67,68].

8. NONLINEAR SUSCEPTIBILITY

A. Second-Order Nonlinear Coefficients of LISe
The elements d_{ij} of the nonlinear tensor have been determined from measurement of the SHG efficiency using either type-I or type-II interactions in the principal planes of LISe and also out of them. Since femtosecond pulses were applied for the SHG, the use of very thin oriented samples of LISe makes it possible to neglect the effects of absorption, beam walk-off, and focusing with the data analysis in the low-depletion limit derived from standard plane-wave SHG theory. That is why care was taken to keep the conversion efficiency low enough in order to avoid complications from saturation effects and spatial effects across the beam cross section.

The coefficient d_{31} was estimated by type-I SHG in the *X-Z* plane from Eq. (16), once it was known it was used for the determination of d_{24} from type-II SHG in the *X-Y* plane with Eq. (14) and assuming Kleinman symmetry to hold (i.e., $d_{15}=d_{31}$). Alternatively the plane *Y-Z* could be used for the determination of d_{24}; however, the spectral tunability is very narrow in this principal plane (see Fig. 14) which is not adequate for measurements with femtosecond pulses. A preliminary measurement of the two nonlinear coefficients d_{31} and d_{24} of LISe by such SHG with femtosecond pulses was presented in [29]. In order to improve the reliability and to extend the results also to d_{33} we repeated it, performing all measurements simultaneously. The diagonal element d_{33} was measured by type-I SHG outside the principal planes, as we previously did for LIS [12], using Eq. (11) and the already determined off-diagonal components of the $d^{(2)}$-tensor, again assuming Kleinman symmetry. The measurements were performed with three annealed LISe samples of yellow color simultaneously with three analogous samples of LIS [12] in order to obtain reliable information on the relative magnitude of the nonlinear coefficients.

All samples had an aperture of 4 mm × 5 mm and were 0.2 mm thick. The LISe samples were cut at $\varphi=0°$ and $\theta=22°$ LISe(1), $\varphi=77°$ and $\theta=90°$ LISe(2), and $\varphi=30°$ and $\theta=27°$ LISe(3). This measurement was relative and we used as a reference sample an AGS crystal with the same dimensions cut at $\varphi=45°$ and $\theta=45°$ for type-I SHG. In order to minimize the error originating from the still different GVM, the pulse width at the fundamental was chosen

relatively large (160 fs in all cases) since LISe samples with thicknesses less than 0.2 mm could not be prepared with sufficient quality. This pulse width corresponds to spectral bandwidths of 80–90 nm. For d_{36} of AGS we used the value of 13.9 pm/V [84] which was measured at a similar wavelength ($\lambda=2.53$ μm). In the plane-wave approximation and having in mind the equal fundamental energy and crystal thickness, d_{eff} of LISe was determined simply from

$$\frac{d_{\text{eff}}^2(\text{LISe})}{d_{\text{eff}}^2(\text{AGS})} = \frac{E_{2\omega}(\text{LISe})}{E_{2\omega}(\text{AGS})} \frac{[1-R(\text{AGS})]^3}{[1-R(\text{LISe})]^3} \frac{n^3(\text{LISe})}{n^3(\text{AGS})}, \quad (19)$$

where n^3 is a product of the three refractive indices involved and R takes into account the Fresnel reflections at the entrance surface (twice for the fundamental) and the exit surface (second harmonic).

The femtosecond source at 1 kHz repetition rate was a KTP-based OPA which was seeded by the frequency-doubled idler of a β-$\beta_a\beta_2O_4$ (BBO)-based OPA, with both OPAs being pumped by the same 800 nm 40 fs pump source (Ti:sapphire regenerative amplifier). The 3 mm KTP used in the OPA ensured sufficiently long wavelengths that cannot be achieved by BBO. Seeding by the frequency-doubled idler of the BBO-OPA was preferred against seeding by the signal wavelength for two reasons: the signal wavelengths available from the BBO-OPA were not short enough to produce idler wavelengths above 2.5 μm with the KTP-OPA, and frequency doubling in a 2 mm thick BBO crystal of the idler used for seeding resulted in temporal broadening and spectral narrowing which was a prerequisite to improve the accuracy. SHG was performed at 2330 nm with LISe(1), 2850 nm with LISe(2), and 2300 nm for LISe(3). In all cases more than 5 μJ at the fundamental were available so that it was possible to reliably measure the SHG with a large area pyroelectric detector even at a low conversion efficiency. We established that up to a conversion efficiency of 20% (energy) into the second harmonic the result did not change. In the case of LISe(3) the polarization angle δ was adjusted by a He-Ne laser monitoring the polarization rotation by the leakage through an analyzer until an eigenmode was reached. No additional improvement of the SHG efficiency could be observed later by further alignment of this angle which was in good agreement with the calculated value from Eq. (13). Note that the dispersion of the optic axis angle V_Z (see Fig. 10) is relatively small and the deviation between visible (633 nm) and 2300 nm is about 10° so that the error originating from that effect is estimated to be less than ±15%. The following results are values of the $d^{(2)}$-tensor components scaled to $\lambda=2300$ nm by using Miller's rule, i.e., assuming same wavelength dispersion of the second-order nonlinearity as for the linear susceptibility:

$$d_{31}(\text{LISe}) = 11.78 \text{ pm/V} \pm 5\%, \quad (20)$$

$$d_{24}(\text{LISe}) = 8.17 \text{ pm/V} \pm 10\%, \quad (21)$$

$$d_{33}(\text{LISe}) = -16 \text{ pm/V} \pm 25\%. \quad (22)$$

The uncertainties are related to the GVM and to the relatively large angular acceptance using thin samples.

The coefficients d_{31} and d_{24} are roughly 10% and 30% higher than in our previous measurement [29] based on different reference materials (AGS and KTP), while d_{33} is measured for the first time. Slightly higher values of d_{31} =12.2 pm/V and d_{32}=10.8 pm/V can be found in [20,52,66] but their origin is unspecified. In the present work we also confirmed the different sign of the diagonal element d_{33} as known for LIS [12]. While the coefficients d_{31} and d_{32} are in the average ≈50% higher than those of LIS [12], the difference between the sulfide and selenide compounds is much smaller if compared to AGS and AGSe [1,2]. The diagonal element d_{33} remains almost unchanged after the substitution of sulfur by selenium [12]. The ratio of d_{24}/d_{31}=0.69 for LISe means that, as for LIS [12], d_{eff} depends only weakly on the azimuthal angle for propagation in the *X-Y* plane.

B. Effective Nonlinearity of LISe

Once the nonlinear coefficients are determined the effective nonlinearity d_{eff} can be easily calculated in the principal planes using Eqs. (12)–(14). As for LIS [12] the maximum d_{eff} is achieved in the *X-Y* plane where it is wavelength (angle) independent because of the similar magnitude of d_{24} and d_{15}. However, as already mentioned in Subsection 7.B, interesting effects can be expected for propagation outside the principal planes due to the high value of d_{33}.

Figure 17(a) shows the calculated $d_{eff}(\varphi, \theta)$ for SHG using Eqs. (11) and (12) with the nonlinearities obtained in the previous subsection and assuming for simplicity a constant V_Z=64° between the optic axes and the
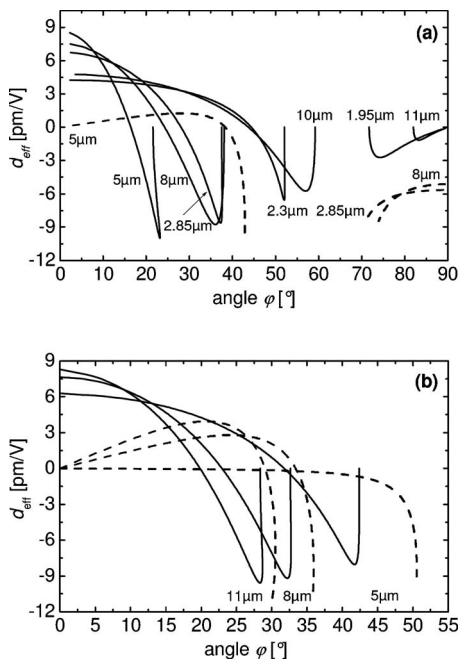

Fig. 17. (a) Effective nonlinearity d_{eff} versus azimuthal angle φ for type-I (*ssf*, solid lines) and type-II (*fsf*, dashed lines) SHGs and (b) downconversion outside the principal planes of LISe. The labels in (a) indicate the fundamental wavelengths corresponding to the (φ, θ) phase-matching loci in Fig. 13. (b), where selected idler wavelengths λ_1=5, 8, 11 μm are shown, is valid for optical parametric generation, amplification, or oscillation with pumping at λ_3=1064 nm.

Z-principal axis (see Fig. 12) which for the wavelengths selected leads to only negligible errors. The fundamental wavelengths indicated in the figure correspond exactly to the phase-matching stereographic projections presented in Fig. 13 where the values for the polar angle θ for the limiting cases φ=0°, 90° can be seen. The curves in Fig. 19(a) start from the *X-Z* plane (φ=0°) and end at the *X-Y* plane (θ=90°) or start from the *X-Y* plane (θ=90°) and end at the *Y-Z* plane (φ=90°). As can be seen from the figure, for type-I SHG in the Hobden classes 9 and 10 (see Subsection 7.A and [72]) the improvement in d_{eff} when propagating outside the principal planes is not significant. For Hobden class 11 the improvement is already significant and for Hobden class 13 it is definitely advantageous to use propagation outside the principal planes for maximum d_{eff} in type-I SHG. In type-II SHG the curves in Fig. 17(a) have a different character and maximum d_{eff} is achieved always in the *X-Y* plane which is advantageous as compared to type-II SHG in the *Y-Z* plane.

For various applications it is important to consider the downconversion into the mid-IR of high-power sources, e.g., lasers emitting at 1064 nm [Fig. 17(b)]. All curves start from the *X-Z* plane (φ=0°), where d_{eff} for type-II interaction (dashed lines) vanishes, and end at the *X-Y* plane (θ=90°), where d_{eff} for type-I interaction (solid lines) vanishes. Calculations in the principal planes for the selected wavelengths indicate that the absolute negative extremum of the type-II d_{eff} curves which occurs in the *X-Y* plane is larger than the extremum of the type-I curves in the *X-Z* plane. Hence the type-II interaction in the *X-Y* plane will be more efficient than the type-I interaction in the *X-Z* plane. However, propagation outside the principal planes allows one to reach a slightly larger maximum $-8 < d_{eff}^{ssf}(\theta, \varphi) < -9.6$ pm/V for the type-I interaction which can be advantageous since other parameters such as the spectral bandwidth can be better in the type-I interaction. We believe the potential for future applications of LISe and LIS [12] in the mid-IR is related also to the utilization of propagation schemes outside the principal planes.

9. PARAMETRIC DOWNCONVERSION

Information on experimental realization of nonlinear optical conversion with LISe is rather scarce. The first nonlinear optical process in LISe was reported in 2001 [29]. The purpose of these SHG experiments in the *X-Y* and *X-Z* planes of LISe, using femtosecond pulses between 2.1 and 2.8 μm, was to test the validity of the existing Sellmeier equations and for preliminary estimations of the nonlinearity. SHG at 9.26 and 9.55 μm was mentioned later in [20,51,53,85] but the phase-matching angle could not be reliably specified. More accurate information on SHG with red color LISe in the 9.2−9.6 μm range was included in [52]. The CO_2 laser SHG efficiency obtained with LISe [51,52,66] shows that this selenide crystal cannot compete with AGSe for this important application: The SHG external efficiency obtained with a 6.2 mm long LISe crystal using 33 ns long pulses was 2.6% in terms of the peak power and 1.5% in terms of energy for a peak pump intensity of 38.5 MW/cm^2 at 9.55 μm, and the ob-

tained second harmonic energy was 7.2 mJ; somewhat higher efficiency, 4.3% in terms of peak power, was reported at 9.26 μm.

In [9] the downconversion of femtosecond pulses from 820 nm to the mid-IR range up to 11 μm was demonstrated for the first time with yellow LISe. In this work LISe was compared to LIS (both samples were uncoated and cut for type-II phase-matching in the X-Y plane, annealed, and 3 mm thick). The OPA was pumped at 820 nm by 220 fs 230 μJ pulses at 1 kHz and the peak on-axis pump intensity was 50 GW/cm^2. It was seeded by continuum generated with $\approx$30 μJ of pump radiation in a 2 mm thick sapphire plate by selecting $\approx$10 nm wide spectral portions with the use of interference filters. Under identical pump and seed conditions, however, the performance of LISe was inferior to that of LIS since the GVM in it is larger and the two-photon absorption (TPA) effect is rather strong. This is a good example of a situation where although the effective nonlinearity is higher, the performance of a given crystal is limited by other factors. In 2005 the first nanosecond OPO based on LISe pumped at 1064 nm was demonstrated [69] but the tunability for the idler, $3.34-3.82$ μm, did not extend beyond 5 μm. Here we will present recent results on two downconversion experiments performed with LISe: DFG in the CW regime and extended nanosecond OPO operation, both of them utilizing its transparency range in the mid-IR.

A. Continuous-Wave Mid-IR DFG
The results of the CW DFG presented here were already partially used in the derivation of the accurate Sellmeier expansions in Subsection 6.A. Such CW DFG, when both light sources have narrow ($<$1 MHz) linewidths, is most suited for high-resolution spectroscopy in the mid-IR range where powers of the order of 1 μW are sufficient to perform sub-Doppler spectroscopy of heavy atmospheric molecules.

Two tunable (from 700 to 810 nm and from 800 to 900 nm) CW single-frequency Ti:sapphire lasers were used in the present experiment as DFG sources (Fig. 18). The laser beams, orthogonally polarized, were collinearly focused onto the crystal with a 35 cm focal length lens, yielding a nearly optimal waist of $w_{3,2}$=55 μm for both pump (ω_3, $k_3=\omega_3 n_3/c$) and signal (ω_2, $k_2=\omega_2 n_2/c$) wavelengths ($\lambda_3 < \lambda_2$). The resulting internal pump and signal wave Rayleigh lengths are $z_3=k_3 w_3^2/2=31$ mm and $z_2=k_2 w_2^2/2=28$ mm, corresponding to nearly equal confocal parameters (ECP) and quasi-plane-wave cylindrical focusing conditions with respective focusing parameters $l_{3,2}=l_c/z_{3,2}$ (l_c denotes the physical crystal length). The in-
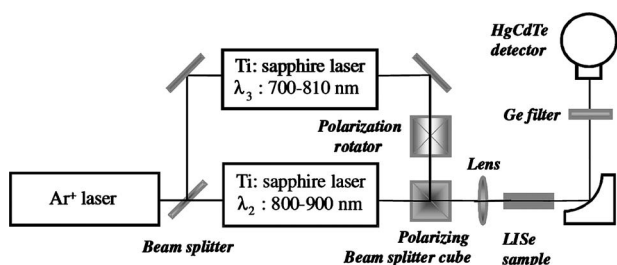
put beams are blocked behind the LISe sample by a 1 mm thick uncoated germanium (Ge) filter, and the mid-IR idler radiation ($\omega_1=\omega_3-\omega_2$, $k_1=\omega_1 n_1/c$) was detected by a calibrated liquid-N$_2$-cooled HgCdTe photoconductive detector fed to a lock-in-amplifier. The LISe sample studied was a l_c=9 mm long uncoated crystal of greenish color with an aperture of 6 mm$\times$7 mm, cut at $\varphi=55°$ in the X-Y plane for type-II *eo-e* interaction. An uncoated sample of LIS (yellowish in color, l_c=10 mm, with dimensions 5 mm$\times$5 mm$\times$10 mm, cut at $\varphi=42°$ in the X-Y plane) served as a reference. In both cases the pump *e*-wave walkoff angle ρ_3 translates into an undimensional walkoff parameter $B=\rho_3[(k_3-k_2)l_c]^{1/2}/2$ while the DFG degeneracy parameter is defined by $\mu=k_2/k_3$ [86]. For LISe, ρ_3=1.051° (18.34 mrad), B=1.26, and μ=0.898 while for LIS the DFG process is characterized by ρ_3=0.97° (16.92 mrad), B=1.19, and μ=0.892.

In a first step, we compared the mid-IR tuning range of LISE and LIS obtained by setting the crystal at normal incidence while tuning simultaneously the pump and signal wavelengths so as to keep $\Delta k=k_3-k_2-k_1\approx 0$ [Fig. 19(a)]. The tuning ranges that were covered with LIS and LISe in the mid-IR were 6.6–7 μm and 6.2–6.8 μm, respectively. These ranges were then extended by angle tuning to 5.5–11.3 μm for LIS and to 5.9–8.1 μm for LISe [Fig. 19(b)]. In these cases λ_2 was fixed at $\approx$836 nm (LIS) and $\approx$807 nm (LISe) and only the input wave at λ_3 was varied. The data presented in Fig. 19(b) correspond to incidence angles in the $-20°$ to $+20°$ range. As could be expected the agreement with the calculated phase-matching curves is excellent because the same experimental data were used in the corresponding Sellmeier sets refinement

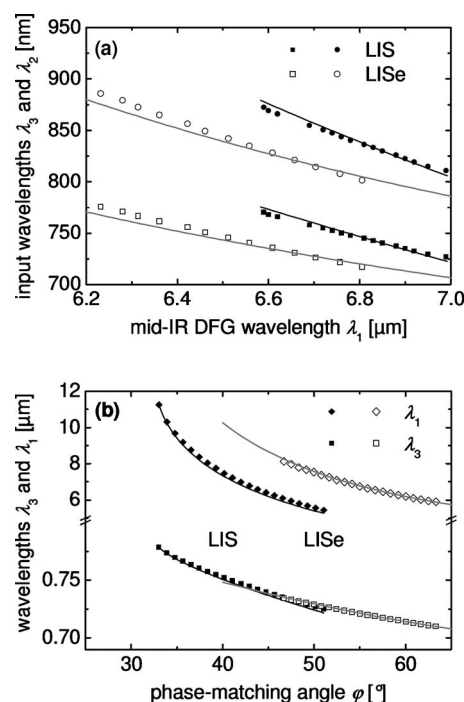Fig. 18.   Schematic of the experimental setup for DFG with LISe.

Fig. 19.   Tunability obtained in the mid-IR with LIS (full symbols, black lines) and LISe (open symbols, gray lines) (a) under normal incidence and (b) when rotating the nonlinear crystals in the X-Y plane. The symbols show the experimentally measured points and the lines are calculated with the Sellmeier equations (Eqs. (7) and (12)).

procedures. It is obvious from Fig. 19(b) that LIS provides a broader tunability range, and longer wavelengths in the mid-IR can be achieved with the given laser sources [87].

The DFG conversion efficiencies recorded at normal incidence and under identical focusing conditions are plotted in Fig. 20 versus the input power product $P_2 P_3$, showing that the conversion efficiency obtained with LISe is higher. The external slope efficiency obtained with LISe was $\Gamma_{exp} = P_1/(P_2 P_3) = 2.7 \ \mu W/W^2$ ($\Gamma_{exp} = 2.4 \ \mu W/W^2$ for LIS). When corrected for all losses (crystal output facet $R \sim 15\%$ and input facet $R \sim 16.5\%$ for each of the input beams), the above conversion efficiency must be multiplied by a factor of ~ 1.7, yielding a net $\Gamma_{net} = \Gamma_{exp}/0.59 \approx 4.6 \ \mu W/W^2$ for LISe.

According to the generalized Gaussian beam theory of undepleted DFG valid for any polarization configuration (type-I or type-II) [69], and taking into account the effect of diffraction, walk-off, material absorption coefficients α_i ($i = 1, 2, 3$), and arbitrary pump/signal waists $w_{3,2}$ with location $f_c = \eta l_c$ measured from the crystal input facet ($0 \leq \eta \leq 1$, with $\eta = 0.5$ corresponding to waists location at the crystal center when $\alpha_i = 0$), the type-II (*eo-e*) DFG power conversion efficiency $\Gamma = P_1/(P_3 P_2)$ under the focused beam expresses as

$$\Gamma = K \exp(-\alpha_1 l_c) l_c (k_2^{-1} - k_3^{-1})^{-1} h(a, l, f, \sigma), \qquad (23)$$

$$
h(a, l, f, \sigma) = \frac{\kappa_e}{2l} \int \int_{-f}^{l-f} d\tau d\tau'
$$
$$
\times \frac{\exp[-a(\tau + \tau' + 2f) + i\sigma(\tau - \tau')]}{(1 + i\kappa_e \tau') Q(\tau) + (1 - i\kappa_e \tau) Q^*(\tau')} F_\beta(\tau, \tau').
$$
$$\qquad (24)$$

The generalized DFG aperture function (24), when applied for a type-I (*oo-e*) interaction and ECPs for both pump and signal ($l_3 = l_2$), reduces to the type-I ECP expression derived by Chu and Broyer [88] as demonstrated in [84]. In Eq. (23), $K = 8\omega_1^2 d_{eff}^2 / \pi \varepsilon_0 c^3 n_1 n_2 n_3$, $a = (\alpha_3 + \alpha_2 - \alpha_1) z_d / 2$, $l = l_c / z_d = (\mu l_2 + l_3)/(1 - \mu)$ is an *effective* focusing parameter ($z_d = (1/2) k_1 w_d^2 \equiv [(k_3 - k_1)/(k_2 z_3 + k_3 z_2)] z_2 z_3$) derived from the individual focusing parameters $l_{3,2} = l_c / z_{3,2}$, $f = f_c / z_d \equiv \eta l$, and $\sigma = \Delta k z_d$ is the normalized wavevector mismatch ($\Delta k = k_3 - k_2 - k_1$). In the expression
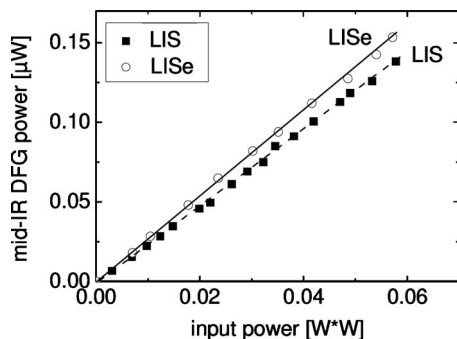

Fig. 20. Dependence of the DFG power at normal incidence ($\lambda_1 = 6.7 \ \mu m$) produced by LISe ($l_c = 9$ mm, $B = 1.26$; circles and solid line) and LIS ($l_c = 10$ mm, $B = 1.19$; squares and dashed line) versus input power and corresponding linear fits for the external slope efficiencies. The conversion efficiencies are corrected only for the uncoated Ge filter transmission loss.

of the DFG Gaussian aperture (or focusing) function h [Eq. (24)], $\kappa_e = [(k_3 - k_2)/(k_2 z_3 + k_3 z_2)]^2 z_2 z_3$ and the function $Q(\tau)$ as well as the walkoff function F_β are given explicitly in [86] ($\beta = \rho_3 z_d / w_d \equiv B \sqrt{2/l}$ is the walkoff angle scaled to the DFG *effective* polarization-wave divergence). Equations (23) and (24) can be in principle used for an absolute determination of the nonlinear effective coefficient d_{eff} of LISe (which is contained in the constant K). Indeed numerically optimizing the aperture function h over σ and η while assuming $\alpha_3 = 0.12$ cm^{-1}, $\alpha_2 = 0.08$ cm^{-1}, $\alpha_1 = 0.04$ cm^{-1} (from the LISe transmission spectra shown in Fig. 3) at $\lambda_3 = 721$ nm, $\lambda_2 = 807$ nm, $\lambda_1 = 6.74 \ \mu m$ yields $h_{opt} = 0.1487 \times 10^{-2}$ with $\sigma_{opt} = -0.26$ and $\eta_{opt} = 0.48$ for the experimental waists $w_{3,2} = 55 \ \mu m$ ($l_3 = 0.289$, $l_2 = 0.322$). The fact that the optimal value of $\sigma = \Delta k z_d$ is not strictly zero is a common feature of Gaussian beam diffraction and walkoff effects in parametric interaction. Despite the strong pump absorption, the optimal relative waist location η derived from the numerical optimization algorithm of h is actually close to but slightly ahead of the crystal center ($\eta = 0.5$) because pump and signal absorption exceeds by far the idler absorption. Let us note that when the DFG focusing function h is optimized with respect to the two individual pump focusing parameters (l_3, l_2) to find the absolute optimum waists w_{3m} and w_{2m} one arrives at $w_{3m} = 39 \ \mu m$ ($l_{3m} = 0.575$) and $w_{2m} = 46 \ \mu m$ ($l_{2m} = 0.462$) with $h_m = 0.1603 \times 10^{-2} = 1.076 h_{opt}$, meaning that despite the slightly larger experimental waist $w_{3,2} = 55 \ \mu m$, the focusing condition is nearly optimum in terms of the aperture function.

Using the calculated h_{opt} in Eq. (23) and the corrected $\Gamma_{net} = 4.6 \ \mu W/W^2$ value, one derives then $d_{eff} = d_{24} \sin^2 \varphi + d_{15} \cos^2 \varphi \sim 6$ pm/V ($\pm 30\%$), while the value expected from Eq. (14) and the nonlinear tensor elements derived from SHG at 2300 nm [Eqs. (20) and (21)] would yield $d_{eff}(\varphi = 55°) = 9.35$ pm/V. The discrepancy originates from the uncertainties in the spatial overlap of the pump waists inside the sample, possible fluctuation of the absorption coefficients for the specific LISe sample used, and possibly also from the implicit theoretical assumption that the walkoff angle at λ_3 is identical to that at λ_1, which is not strictly the case due to normal dispersion of LISe.

The DFG nonlinear coefficient of LISe can also be derived as a relative measurement with respect to LIS (taken as a reference material), by taking the experimental ratio $\Gamma_{LISe}/\Gamma_{LIS} = 1.12$ from Fig. 20. Relative measurements are expected to be less subject to the above experimental uncertainties; all more than the refractive indices of LISe and LIS are quite close. If one assumes nearly identical absorption loss at λ_1 for LIS and LISe and nearly identical indices of refraction, Eqs. (23) and (24) lead to

$$
\frac{\Gamma_{LISe}}{\Gamma_{LIS}} \approx \frac{[\lambda_2 - \lambda_3]_{LIS}}{[\lambda_2 - \lambda_3]_{LISe}} \frac{[d_{eff}^2 l_c h(B)]_{LISe}}{[d_{eff}^2 l_c h(B)]_{LIS}}
$$
$$
= 0.84 \frac{[d_{eff}^2]_{LISe}}{[d_{eff}^2]_{LIS}} \frac{[h(B)]_{LISe}}{[h(B)]_{LIS}}. \qquad (25)
$$

The last factor in Eq. (25) takes into account the different walkoff parameters $B = 1.26$ for LISe and $B = 1.19$ for

LIS in the evaluation of the focusing functions $h(B)$, yielding $[h(B)]_{LISe}/[h(B)]_{LIS}=0.1487\times10^{-2}/0.1926\times10^{-2}=0.772$. It can be concluded from Eq. (25) that $d_{eff}(LISe)\approx1.32d_{eff}(LIS)$. This is in fair agreement with the estimated ratio from Eqs. (20) and (21) and [8,12] which is $d_{eff}(LISe)=(1.35-1.43)d_{eff}(LIS)$. Using the nonlinear tensor elements for LIS determined in [8,12] which yield $[d_{eff}(\varphi=42°)]_{LIS}=6.54$ pm/V ($\pm30\%$), the effective nonlinear coefficient of LISe determined by this relative measurement is $d_{eff}(\varphi=55°)=8.63$ pm/V ($\pm30\%$), much closer to $d_{eff}=9.35$ pm/V as calculated with the tensor elements determined from SHG in Eqs. (20) and (21). The slight deviation can be attributed to the slightly larger index of refraction of LISe which was not taken into account above.

The DFG spectral tuning characteristics in the case of LISe (at normal incidence) are shown in Fig. 21(a) with a thick solid line. In this case, the fixed wavelength was $\lambda_2=807.2$ nm and λ_3 was varied near 721 nm. The angular DFG acceptance curves (at fixed $\lambda_3=721$ nm and $\lambda_2=807.2$ nm) are plotted in Fig. 21(b). In both figure parts, the dashed lines are the calculated *plane-wave* [proportional to $sinc^2(\Delta kl_c/2)$] acceptance curves.

The fact that the experimental acceptance bandwidths are broader than the bandwidths calculated with the simple plane-wave formula [$\Delta\varphi=0.13°$ in Fig. 21(b)] can be attributed to the effects of spatial walk-off and focusing which reduce the actual interaction lengths. The thin solid lines are the Gaussian beam spectral and angular acceptance curves computed using $h(\sigma)$ [Eq. (24)], where in the normalized phase-mismatch parameter $\sigma=\Delta kz_d$,

$\Delta k(\lambda_i,\varphi)$ has been evaluated using the Sellmeier dispersion relation of LISe [Eqs. (7)]. In computing $\Delta k(\lambda_3,\lambda_1)$ for the spectral acceptance, the energy conservation was taken into account ($\omega_3=\omega_2+\omega_1$). Note that the slight asymmetry observed in the Gaussian-wave acceptance curves $h(\sigma)$ in Fig. 21 is due to the combined effect of focusing and beam walk-off [86].

B. Pulsed Nanosecond OPO

At practical pump intensities, most of the chalcogenide mid-IR nonlinear crystals will suffer TPA under pulsed pumping at 1064 nm because of their low bandgap. In fact, there are only few candidates for such downconversion devices pumped near 1064 nm, the properties of which were compared in [89] taking into account the TPA, residual absorption, birefringence, effective nonlinearity, thermal conductivity, and limitations related to the growth, availability, and some opto-mechanical properties. The most impressive nanosecond OPO results so far have been achieved with AGS, for which idler tunability from 3.9 to 11.3 μm was demonstrated [90]. CSP is also a very promising candidate for such an OPO [3] but a practical upper limit of 6.5 μm for the idler wavelength is set for it by intrinsic multi-phonon absorption: This defines a potentially interesting spectral range of only 4−6.5 μm. The interest in LISe is motivated by its superior thermomechanical properties in comparison to AGS: isotropic expansion, thermal conductivity, and smaller thermo-optic coefficients as well as higher damage threshold, which are important for average power scaling.

The experimental setup with the OPO cavity is shown in Fig. 22 [91]. It consisted of two plane mirrors with a
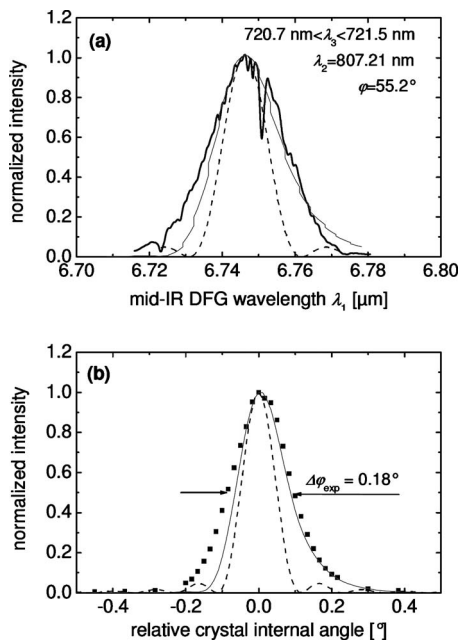

Fig. 21. (a) Measured (thick solid line) and calculated by plane-wave model (dashed line) phase-matching characteristics for mid-IR DFG with LISe when tuning only one of the input wavelengths at a fixed phase-matching angle. Water-vapor absorption lines are observed since the path to the detector was not evacuated. The thin solid line is the result of the Gaussian beam theory. (b) Angular acceptance of DFG near $\lambda_1=6.7$ μm. The symbols show the experimental data, the dashed line shows the plane-wave model, and the thin solid line shows the Gaussian beam theoretical $h(\sigma)$ normalized pattern.
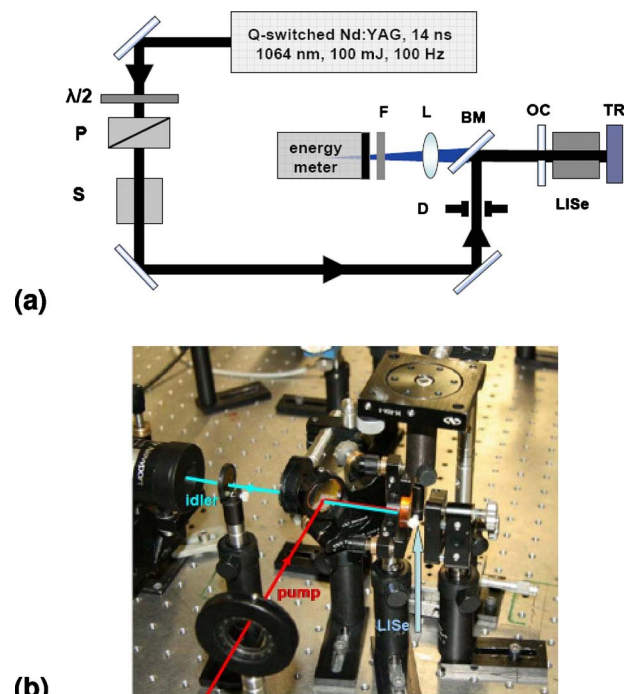

Fig. 22. (Color online) (a) Experimental setup of the LISe OPO: $\lambda/2$, half-wave plate; P, polarizer; S, mechanical shutter; F, 2.5 μm cut-on filter; L, 10 cm MgF$_2$ lens; D, diaphragm; BM, bending mirror; OC, output coupler; TR, total reflector. (b) Photograph of the compact OPO setup.

separation between 18.5 and 27.5 mm, depending on the LISe crystal used. The rear total reflector, TR, was an Ag-mirror (Balzers) with a reflection of >98.5% at the pump, signal, and idler wavelengths. In the tuning range studied in the present work, the output coupler, OC, had a transmission of 18%–22% at the signal and ∼73%–84% at the idler wavelength; hence, the OPO can be considered as singly resonant with double pass pumping. However, the signal was not totally reflected by the output coupler to avoid extreme intracavity fluence that could damage the crystals. The LISe crystals were pumped through the output mirror which had a transmission of 82% at 1064 nm. The beams were separated by the pump bending mirror, BM, which had high reflection for the pump ($R=98\%$ for p-polarization) and transmitted ∼67% (p-polarization) at the idler wavelengths. Both the plane-parallel output coupler, OC, and the bending mirror, BM, were on ZnSe substrates with uncoated rear surfaces.

The pump source was a diode-pumped electro-optically Q-switched Nd:YAG laser (Innolas GmbH, Germany) optimized for a repetition rate of 100 Hz. According to the specifications, its linewidth amounts to 1 cm^{-1}, M^2 is <1.5, and the divergence is <0.5 mrad. The laser generated 100 mJ 14 ns (FWHM) pulses with an average power of 10 W. The measured energy stability was ±1%.

A mechanical shutter (S) with an aperture of 8 mm, operating up to 50 Hz (nmLaser), was employed to reduce the repetition rate and thus the average pump power. A combination of a half-wave plate, $\lambda/2$, and a polarizer, P, served to adjust the pump energy. The pump laser was protected by a Faraday isolator and the separation to the OPO was large enough to avoid feedback during the Q-switching process. The pump beam was not focused and had a Gaussian waist of $w \sim 1.9$ mm in the position of the OPO. The output of the OPO, behind the bending mirror, BM, was detected by a calibrated pyroelectric energy meter positioned in front of the focus of a 10 cm MgF$_2$ lens, L. Only the idler energy was measured; the residual pump radiation and the signal were blocked by a 2.5 μm cut-on filter, F.

The samples used in the present study were unfortunately from old growth experience and exhibited substantial residual absorption. They were cut for propagation in the X-Y plane, type-II e-oe phase-matching, which is characterized by maximum effective nonlinearity. One sample (A) was cut at $\varphi=41.6°$ for idler wavelength ∼6.5 μm at normal incidence. It had an aperture of 5 mm (along the Z-axis) $\times 6.5$ mm and a length of 17.6 mm. This sample was antireflection (AR)-coated with a single layer of YF$_3$ for high transmission at 1064 nm and in the 1.15–1.35 μm signal range. We measured average surface reflectivity of 2.8% at 1064 nm and 1.8% at 1600 nm. From the measured transmission of 71% at 1064 nm and 85% at 1600 nm, we estimated effective absorption (including scatter) of 16%/cm at 1064 nm and 7%/cm at 1600 nm.

The second sample (B) was cut at $\varphi=34°$ for the idler wavelength of ∼8.8 μm at normal incidence. It had an aperture of 5 mm (along the Z-axis) $\times 7$ mm and a length of 24.5 mm. This sample was AR-coated with the same single layer for high transmission at 1064 nm and in the 1.15–1.35 μm signal range. However, due to some failure

in the coating process, the difference in the residual reflectivity of the two surfaces was more pronounced. One surface had substantially higher (5% at 1064 nm and 4.5% at 1600 nm) reflection than the other (1% at 1064 nm and <1% at 1600 nm). From the measured transmission of 67.7% at 1064 nm and 82% at 1600 nm, we estimated for sample B effective absorption (including scatter) of 14%/cm at 1064 nm and 6%/cm at 1600 nm, which are very similar to the estimates for sample A.

We studied the input/output characteristics of the OPO, including the oscillation threshold, at normal incidence and minimum possible cavity length. The tuning curve required tilting of the crystal and the corresponding cavity length was slightly increased.

The thresholds measured for cavity lengths of 18.5 mm (sample A) and 25.5 mm (sample B) amounted to 6.8 and 7.9 mJ energies incident on the crystals, respectively. These values correspond to average fluences of 0.06 and 0.07 J/cm^2 or pump intensities of 4.3 and 5 MW/cm^2. The peak on-axis values for the fluence and the intensity are two times higher. The threshold can be calculated by using Brosnan and Byer's formula [92] for a singly resonant OPO with recycled pump. We used the exact experimental parameters, correcting for the pump beam absorption after the first pass and assuming equal (averaged for signal and idler) absorption of 5%/cm^{-1} for the resonated wave. From the nonlinear coefficients of LISe, rescaled using Miller's rule, we calculated effective nonlinearities of $d_{\mathrm{eff}}=10.6$ pm/V ($\varphi=41.6°$, sample A) and 11 pm/V ($\varphi=34°$, sample B) (see Table 1). The results for the threshold pump fluences were 0.23 and 0.15 J/cm^2 for samples A and B, respectively. These values correlate better with the experimental peak (on-axial) values which can be explained by the fact that oscillation starts in the central part of the pump beam. Deviations and the fact that sample B had in fact a higher oscillation threshold than sample A may have several reasons: the losses at the exact signal and idler wavelengths were unknown and we interpolated them to 6% cm^{-1} at the signal and assumed 4% cm^{-1} at the idler wavelength in accordance with [69]; eventually these losses, in particular for sample B, could be higher. Besides, for the pump, the residual reflections at the crystal faces were neglected; and finally the partial resonance of the idler is not taken into account by the theory. Having in mind all such assumptions, the correspondence between theory and experiment can be considered as satisfactory.

At a pump level of about two times the pump threshold we investigated the dependence of the output power on the repetition rate in the range 10–100 Hz. Fluctuations were within the experimental error and we conclude that there is no such dependence. This result was rather unexpected since the present samples had in fact larger residual absorption than the one used in the initial work [69] at shorter idler wavelengths. This fact can be explained by the weaker thermal lensing in the case of larger beam sizes. The measurements were performed at 100 Hz with the shutter removed [Fig. 22(a)].

The input/output characteristics for the two samples are shown in Fig. 23(a). Maximum energies of 282 μJ at 6.514 μm and 116 μJ at 8.428 μm were measured. These values correspond to external quantum conversion effi-
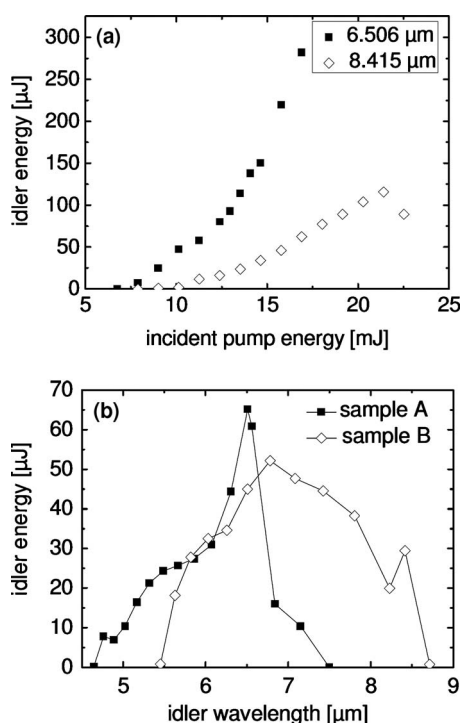
Fig. 23. (a) Output idler energy with LISe sample A (squares) and sample B (diamonds) versus pump energy at 1064 nm, incident on the crystals. The curves are recorded at normal incidence with cavity lengths of 18.5 and 25.5 mm, respectively. The last point in case B denotes a surface damage. (b) Tuning OPO curves recorded for the two LISe samples at fixed pump energy.

ciencies of 10.3% and 4.3%, respectively. The above wavelengths deviate from the calculated ones being longer for sample A and shorter for sample B. However, the deviations at the signal wavelengths, from the measurement of which the idler wavelengths were calculated, were only about 3 and 5 nm, respectively. The maximum average power at 100 Hz amounts to 28 mW. This is an improvement of more than 1 order of magnitude in comparison to our initial work, where ~2.5 mW at 3457 nm were achieved at lower repetition rates [69]. This compares well with 372 μJ at 6 μm reported with an AGS OPO [90]. Since the OPO operation with any chalcogenide crystal is confined to a narrow pump power range between the oscillation and damage thresholds this fact emphasizes the importance of the good spatial profile and the pulse-to-pulse stability of the diode-pumped pump source.

The OPO linewidth was measured at the signal wavelength of 1272 nm using a 1 mm thick Ag-coated CaF$_2$ Fabry–Perot etalon. It was ~58 GHz (~1.9 cm^{-1}). This is two times less than the spectral acceptance for the three-wave nonlinear process assuming a narrowband pump. The pulse-to-pulse stability for the idler pulses measured at the maximum output level was ±5%. The pulse duration at the same signal wavelength, measured with a fast (0.7 ns) InGaAs photodiode, was 7 ns.

The tuning curves [Fig. 23(b)] were recorded by lengthening the cavity to 20.5 mm (sample A) and 27.5 mm (sample B) and tilting the crystals in the critical plane (rotation about the *z*-axis). The pump energies were 11.8 mJ for sample A and 16.9 mJ for sample B. Note that the upper limit of the tunability is determined by the LISe ab-

sorption which, for such sample lengths, sets on from about 8 μm, and is not related to the optics used (the thin MgF$_2$ lens was substituted by a BaF$_2$ lens to check this). The point which deviates from the smooth dependence for sample B is near 8.428 μm, corresponding to normal incidence, which can be explained by some enhancement of the feedback by the partial reflection of the crystal faces.

Thus we showed that the full transparency range of LISe can be utilized using an OPO pumped at 1064 nm; however, in order to extend the tunability up to 12 μm and more, shorter crystal samples will be needed in addition to reduced residual crystal loss. This in turn means that the OPO should be operated at higher pump levels which will require solution of the surface damage problem. The average power obtained with LISe (28 mW) substantially exceeds the levels achieved with AGS (3.7 mW in [90]) and CSP (9.1 mW in [3]) at similar wavelengths but at lower repetition rates.

10. LASER-INDUCED DAMAGE IN LISe

Surface damage of LISe was observed with both OPO active elements and studied also with four 1 mm thick plates, cut in the same direction as sample B. Two of these plates were only polished and the other two had AR-coating on one of their faces only. The results of the extracavity damage tests at 1064 nm using the same pump source without focusing can be summarized as follows.

For uncoated and AR-coated LISe plates, complete damage (surface and crack) occurs for 14 ns long pulses at 1064 nm and 100 Hz within seconds/minutes for 44–52 mJ incident energy, with on-axis fluence of 0.78−0.92 J/cm^2 (56−66 MW/cm^2 peak on-axis pump intensity). In several cases irreversible whitened spots (surface deterioration) were observed starting from 29 mJ, corresponding to an on-axis fluence of 0.5 J/cm^2 or a peak on-axis intensity of 36 MW/cm^2. This is the minimum fluence value for which such kind of damage was observed, and there is obvious dependence on the position and the sample. For increasing pump levels, the whiter spots changed slightly in diameter and preserved their color, until complete damage occurred. The whiter spots appear on uncoated surfaces; however, they occur also on AR-coated surfaces, presumably beneath the layer. In most of the cases they occurred at higher pump energies and in one of the uncoated test plates they did not occur at all, until complete damage was observed at 52 mJ [Fig. 24(b)], which seems to indicate that this effect is related to the polishing/coating procedure since all samples were from the same LISe boule.

In principle the AR-coating applied seems to be sufficiently resistant for the OPO operation and in some cases the surface damage threshold was higher for the AR-coated surface. But the quality of the coating is not reproducible as evidenced in the OPO experiment, in which always one of the surfaces (the one with higher residual reflection) got damaged at lower pump levels, independent of whether it was a front or rear surface with respect to the pump.

The lowest pump level at which surface damage to the OPO sample A in the form of whitened spots on the coating (or beneath it) was observed was a peak on-axial
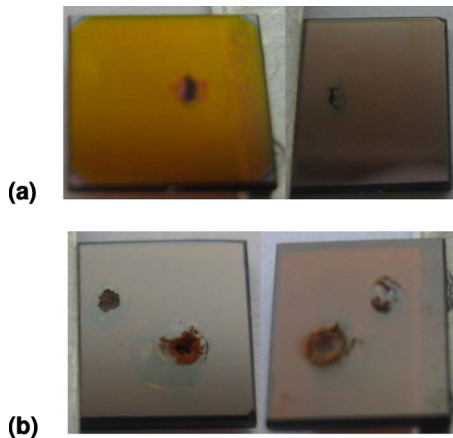
Fig. 24.   (Color online) (a) Damage of the AR-coated front surface (left) and the uncoated rear surface (right) of a LISe test plate after illumination with 3000 pulses of 50 mJ energy and (b) damage of both sides of an uncoated LISe test plate at 52 mJ single pulse energy after 3000 (small spots) and 10,000 (large spots) pulses.

pump intensity of 16 MW/cm^2. This corresponds to operation roughly two times above the threshold and strong signal field is already present in the cavity. By translating the sample in the transversal direction, we observed several times the same kind of damage to the same surface, the one with higher residual reflectivity of the AR-coating, independent of the orientation of the sample with respect to the pump beam (entrance or exit surface). No damage occurred to the other surface of the sample.

The same sample A was studied for damage also extracavity using the same pump source and fresh positions. The tests were performed for 60 s (6000 shots). Again the same surface had a low damage threshold although it was always an exit surface. The damage threshold for the occurrence of similar whitened spots was 23 MW/cm^2. Full damage to this surface [coating destroyed and crater appeared; see Fig. 25(a)] occurred at 45 MW/cm^2. At this same intensity level, the first whitened spot on the other surface (the one with lower residual reflectivity) was observed.

It can be only speculated why damage of the two OPO samples in the form of whiter surface spot occurred at much lower pump energy (10–15 mJ) when inside the cavity. Nevertheless, the presence of such spots did not affect the OPO performance until the damage developed further as can be seen from Fig. 23(a). Complete damage was also observed at lower levels (15–20 mJ) inside the cavity but could be a consequence of already existing whiter spot. There are two possibilities: either contribution from the resonated signal wave (as reported for other crystals [90])
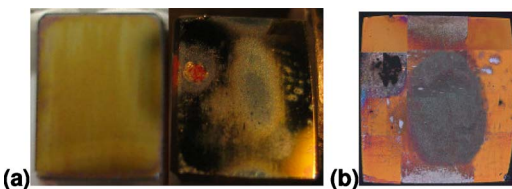

Fig. 25.   (Color online) (a) Lower-reflecting (left) and higher-reflecting (right) surface of the damaged LISe OPO element and (b) 12 microscope images of the severely damaged higher-reflecting surface combined into a single picture.

or simply low quality of this AR-coating. Experiments outside the cavity indicated lower damage of the surface with higher residual reflection, also lower threshold for whitening, so it seems more probable that this surface was simply of lower quality and that is why it got damaged although it was not always the front surface in the OPO. The different damage resistivities of the two surfaces could be attributed to the fact that after AR-coating one of the surfaces, the other one was not repolished. In the future we plan to polish the two crystal faces independently prior to their coating. Comparing the results with coated and uncoated surfaces one can expect that, for the present quality of the grown material, optimization of the AR-coating process could allow the safe use of peak on-axis intensities of about 50 MW/cm^2 or incident pump energy of roughly 40 mJ. Once the problem with the reproducibility of the AR-coating is solved one can expect substantial improvement of the OPO performance.

For other types of OPOs pumped by mode-locked lasers near 1 μm (synchronously pumped OPOs) which operate at ~100 MHz repetition rates, it is essential to know the CW optical damage threshold of LISe. To this aim we tested one of the uncoated 1 mm thick plates with a CW Nd:YVO$_4$ laser operating at 1064 nm. With a 30 mm best shape lens we measured a waist diameter in the focus of $2w_0 = 18$ μm and estimated $M^2 = 1.6$. The maximum power applied, measured after the lens, was 8.5 W which gives an average intensity of 3.3 MW/cm^2 in the focus. By translating the plate through the focus and averaging two tests we estimated then a damage threshold of ~6 MW/cm^2 in terms of the peak on-axis intensity. The bulk damage was in the form of dark spots inside the sample.

In the mid-IR, the optical damage of LISe has been characterized by others with 30 ns long single pulses at 9.55 μm, with the result of 241–248 MW/cm^2 [20,52]. Using femtosecond pulses at 820 nm (220 fs, 1 kHz), the first damage phenomenon, partially reversible, was gray track formation in the bulk at about 55 GW/cm^2 [9], in contrast to the nanosecond OPO experiments in which such an effect was not observed at 1064 nm [91].

TPA was measured below this intensity, as shown in Fig. 26, for a 3 mm thick yellow LISe sample ($\varphi = 52°$ cut in the *X-Y* plane). The experimental data were averaged for the two possible polarization orientations and then fitted assuming Gaussian temporal and spatial beam profiles. Taking into account a linear absorption of 0.5 cm^{-1} at this wavelength, the result for the TPA coefficient was 0.6 cm/GW.
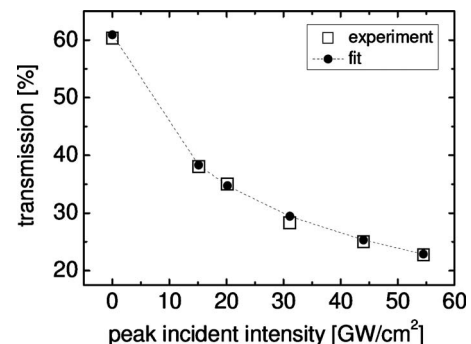

Fig. 26.   TPA in LISe: experimental data and theoretical fit.

11. MISCELLANEOUS APPLICATIONS OF LISe AND SUMMARY OF PROPERTIES

Finally, we would like to outline that the epitaxial growth of LISe films was demonstrated on Si, GaAs, GaP, and CaF$_2$ [93–97]. In [98] electroluminescence from LISe–GaP heterodiodes (*p*-type LISe-film on *n*-type GaP) was observed near 610 nm. The system Cu$_{1-x}$Li$_x$InSe$_2$ which exhibits a transition from chalcopyrite to β-NaFeO$_2$ structure has also been studied [17,99–101], thin films of it were deposited on GaAs [102] and their optical properties were investigated [103]. Narrowband terahertz emission from LISe has been observed in [104] under femtosecond excitation at 1560 nm. Table 6 summarizes the known properties of LISe, a great part of them characterized in the present work.

12. CONCLUSION

We have characterized the main physical properties of the newly emerging lithium selenoindate chalcogenide semiconductor that are relevant for nonlinear applications from the visible up to the deep mid-IR. Table 6 summarizes these properties, as well as those determined in previous works. LiInSe$_2$ (LISe) can now be considered as a mature compound, and its future widespread use in nonlinear devices should refine all the data collected from this investigation campaign. Among its most relevant advantages over the existing mid-IR crystals, one may quote its excellent thermal stability and high damage threshold suitable for high-power laser applications and its extremely extended phase-matching capabilities (over its whole transparency range) using either type-I or type-II

Table 6. Summary of Known Crystallographic, Optical, Thermal, and Electrical Properties of LISe

Crystallographic Data	
Structure	Wurtzite-type (β-NaFeO$_2$)
Symmetry, point group	Orthorhombic, $mm2$ (negative biaxial)
Space group	$Pna2_1$
Lattice parameters	$a \approx 7.2$ Å, $b \approx 8.4$ Å, $c \approx 6.8$ Å, $Z=4$
Principal axis assignment	$(X,Y,Z) \leftrightarrow (b,a,c)$
Density (g/cm^3)	4.47
Microhardness (GPa)^a	1.75 ± 0.04
Optical Properties	
Optical transmission	0.54–10 μm (50% level for 10 mm thickness), 0.5–13 μm ("0" level)
Bandgap at 300 K (eV)	2.86
Indices of refraction at 300 K:	
$\lambda = 632.8$ nm	$n_X = 2.387$, $n_Y = 2.435$, $n_Z = 2.437$
$\lambda = 1.064$ μm	$n_X = 2.290$, $n_Y = 2.330$, $n_Z = 2.339$
$\lambda = 10.6$ μm	$n_X = 2.209$, $n_Y = 2.245$, $n_Z = 2.246$
Optical axis angles (0.65 μm $< \lambda <$ 12 μm)	$63° < V_Z < 78°$
Birefringence walk-off at 1064 nm (mrad)	$\rho_{X-Y} = 17.3$, $\rho_{X-Z} = 21.2$
SHG fundamental wavelength range (nm)	1860–11071
Thermo-optic coefficients (10^{-5}/°C) at 1064 nm, 300 K	dn_X/d$T = 5.676$, dn_Y/d$T = 9.339$, dn_Z/d$T = 7.368$
Absorption coefficient at 1.064 μm (cm^{-1})	2%
Laser damage threshold:	
1064 nm, 10 ns, 10 Hz (GW/cm^2), surface damage	~ 0.04
820 nm, 220 fs, 1 kHz (GW/cm^2), gray tracks	~ 55
9.55 μm, 30 ns, single pulse (GW/cm^2)	~ 0.25
1064 nm, CW (GW/cm^2)	~ 0.006
TPA at 0.82 μm (cm/GW), 220 fs	0.6
Nonlinear optical coefficients (pm/V) at 2.3 μm (fundamental)	$d_{31} = 11.78 \pm 5\%$, $d_{24} = 8.17 \pm 10\%$, $d_{33} = -16 \pm 25\%$
Thermal Properties	
Melting point (°C)	915 ± 5
Thermal expansion at 300 K (10^{-5}/K)	$\alpha_X = 1.76 \pm 0.18$, $\alpha_Y = 1.1 \pm 0.16$, $\alpha_Z = 0.87 \pm 0.11$
Specific heat at 300 K [J/(mol K)]	98.1 ± 1.4
Thermal conductivity at 300 K [W/(m K)]	$K_X = 4.7 \pm 0.2$, $K_Y = 4.7 \pm 0.2$, $K_Z = 5.5 \pm 0.3$
Electrical Properties	
Pyroelectric coefficient at 300 K (μC/m^2 K)	16
Pure electro-optic coefficients (relative to LiInS$_2$)	r_{c1}(LISe) $\approx 2.1 r_{c1}$(LIS), r_{c2}(LISe) $\approx 2.6 r_{c2}$(LIS)
Electric conductivity at 300 K (10^{-12} Ω^{-1} cm^{-1})	$\sigma_X \approx 3$, $\sigma_Y \approx 0.08$, $\sigma_Z \approx 0.02$

^{a}From averaging of ten dynamic indentation measurements with 1 μm indentation depth performed on a $\theta = 90°$, $\varphi = 34°$ oriented sample.

interactions in or out of principal planes. Such an extended phase-matching capability is still compatible with low birefringence walkoff angles. LISe exhibits effective nonlinearity higher than that of the related LIS and comparable to that of AGS. Taking into account its similar transparency range, LISe seems to be a good candidate for 1.064 μm pumped mid-IR OPO operation with the advantages of higher thermal conductivity and damage threshold and such results were presented in the present study.

ACKNOWLEDGMENTS

REFERENCES

1. D. N. Nikogosyan, *Nonlinear Optical Crystals: A Complete Survey* (Springer, 2005).
2. V. G. Dmitriev, G. G. Gurzadyan, and D. N. Nikogosyan, *Handbook of Nonlinear Optical Crystals*, 3rd revised ed. (Springer, 1999).
3. V. Petrov, P. G. Schunemann, K. T. Zawilski, and T. M. Pollak, "Non-critical singly resonant OPO operation near 6.2 μm based on a CdSiP$_2$ crystal pumped at 1064 nm," Opt. Lett. **34**, 2399–2401 (2009).
4. P. S. Kuo and M. M. Fejer, "Microstructured semiconductors for mid-infrared nonlinear optics," in *Mid-Infrared Coherent Sources and Applications*, NATO Science for Peace and Security Series B: Physics and Biophysics, M. Ebrahim-Zadeh and I. Sorokina, eds. (Springer, 2008), pp. 149–168.
5. V. Petrov, V. L. Panyutin, A. Tyazhev, G. Marchev, A. I. Zagumennyi, F. Rotermund, and F. Noack, "GaS$_{0.4}$Se$_{0.6}$: relevant properties and potential for 1064 nm pumped mid-IR OPOs and OPGs operating above 5 μm ," Laser Phys. (to be published in 2011).
6. V. Petrov, V. Badikov, and V. Panyutin, "Quaternary nonlinear optical crystals for the mid-infrared spectral range from 5 to 12 micron," in *Mid-Infrared Coherent Sources and Applications*, NATO Science for Peace and Security Series B: Physics and Biophysics, M. Ebrahim-Zadeh and I. Sorokina, eds. (Springer, 2008), pp. 105–147.
7. V. Badikov, K. Mitin, F. Noack, V. Panyutin, V. Petrov, A. Seryogin, and G. Shevyrdyaeva, "Orthorhombic nonlinear crystals of Ag$_x$Ga$_x$Ge$_{1-x}$Se$_2$ for the mid-infrared spectral range," Opt. Mater. **31**, 590–597 (2009).
8. J.-J. Zondy, V. Petrov, A. Yelisseyev, L. Isaenko, and S. Lobanov, "Orthorhombic crystals of lithium thioindate and selenoindate for nonlinear optics in the mid-IR," in *Mid-Infrared Coherent Sources and Applications*, NATO Science for Peace and Security Series B: Physics and Biophysics, M. Ebrahim-Zadeh and I. Sorokina, eds. (Springer, 2008), pp. 67–104.
9. V. Petrov, A. Yelisseyev, L. Isaenko, S. Lobanov, A. Titov, and J.-J. Zondy, "Second harmonic generation and optical parametric amplification in the mid-IR with orthorhombicbiaxial crystals LiGaS$_2$ and LiGaSe$_2$," Appl. Phys. B **78**, 543–546 (2004).
10. L. Isaenko, P. Krinitsin, V. Vedenyapin, A. Yelisseyev, A. Merkulov, J.-J. Zondy, and V. Petrov, "LiGaTe$_2$: A new highly nonlinear chalcopyrite optical crystal for the mid-IR," Cryst. Growth Des. **5**, 1325–1329 (2005).
11. L. Isaenko, A. Yelisseyev, S. Lobanov, P. Krinitsin, V. Petrov, and J.-J. Zondy, "Ternary chalcogenides LiBC$_2$ (B =In, Ga; C=S, Se, Te) for mid-IR nonlinear optics," J. Non-Cryst. Solids **352**, 2439–2443 (2006).
12. S. Fossier, S. Salaün, J. Mangin, O. Bidault, I. Thenot, J.-J. Zondy, W. Chen, F. Rotermund, V. Petrov, P. Petrov, J. Henningsen, A. Yelisseyev, L. Isaenko, S. Lobanov, O. Balachninaite, G. Slekys, and V. Sirutkaitis, "Optical, vibrational, thermal, electrical, damage and phase-matching properties of lithium thioindate," J. Opt. Soc. Am. B **21**, 1981–2007 (2004).
13. T. J. Negran, H. M. Kasper, and A. M. Glass, "Pyroelectric and electrooptic effects in LiInS$_2$ and LiInSe$_2$," Mater. Res. Bull. **8**, 743–748 (1973).
14. T. Kamijoh and K. Kuriyama, "Single crystal growth and characterization of LiInSe$_2$," J. Cryst. Growth **51**, 6–10 (1981).
15. T. Kamijoh, T. Nozaki, and K. Kuriyama, "A photoluminescence study on lithium ternary compounds," Nuovo Cimento Soc. Ital. Fis. **2D**, 2029–2033 (1983).
16. S. Weise, E. Nowak, B. Schumann, and V. Krämer, "LiInSe$_2$ and phase relations in the ternary system Li–In–Se," Cryst. Res. Technol. **31**, Suppl. 31, 817–820 (1996).
17. S. Weise, "Züchtung und Charakterisierung von Kristallen im System Li$_2$Se–In$_2$Se$_3$," Ph.D. dissertation (Albert-Ludwigs-Universität, 2000); www.shaker-online.com.
18. S. Weise and V. Krämer, "Phase study of the system Li$_2$Se–In$_2$Se$_3$," J. Therm Anal. Calorim. **71**, 1035–1038 (2003).
19. V. V. Badikov, V. I. Chizhikov, V. V. Efimenko, T. D. Efimenko, V. L. Panyutin, G. S. Shevyrdyaeva, and S. I. Scherbakov, "Optical properties of lithium indium selenide," Opt. Mater. **23**, 575–581 (2003).
20. Yu. M. Andreev, V. V. Atuchin, P. P. Geiko, V. V. Popov, G. V. Lanskii, and N. C. Trocenco, "New mixed LiIn(S$_{1-x}$Se$_x$)$_2$ crystals for frequency conversion of IR lasers," Proc. SPIE **5743**, 420–427 (2004).
21. Yu. M. Andreev, V. V. Atuchin, G. V. Lanskii, N. V. Pervukhina, V. V. Popov, and N. C. Trocenko, "Linear optical properties of LiIn(S$_{1-x}$Se$_x$)$_2$ crystals and tuning of phase matching conditions," Solid State Sci. **7**, 1188–1193 (2005).
22. L. Isaenko, I. Vasilyeva, A. Merkulov, A. Yelisseyev, and S. Lobanov, "Growth of new nonlinear crystals LiMX$_2$ (M=Al, In, Ga; X=S, Se, Te) for mid-IR optics," J. Cryst. Growth **275**, 217–223 (2005).
23. Z. Z. Kish, E. Yu. Peresh, V. B. Lazarev, and E. E. Semrad, "Systematics and the rules of variations in the properties of A^{I}B^{III}C$_2^{VI}$-type compounds," Inorg. Mater. **23**, 697–703 (1987) [in Russian, Izv. Akad. Nauk SSSR, Neorg. Mater. **23**, 777–784 (1987)].
24. I. G. Vasilyeva and R. E. Nikolaev, "High-temperature solid-vapor and liquid-vapor transitions in binary and ternary chalcogenides La$_2$S$_3$, MoS$_2$, Mo$_2$S$_3$ and LiInSe$_2$," J. Alloys Compd. **452**, 89–93 (2008).
25. I. G. Vasilyeva, R. E. Nikolaev, V. V. Malakhov, and L. I. Isaenko, "Effects of evaporation and melting on nonstoichiometry and inhomogeneity of LiInSe$_2$ crystals," J. Therm Anal. Calorim. **90**, 601–605 (2007).
26. L. I. Isaenko and I. G. Vasilyeva, "Nonlinear Li^{I}B^{III}C$_2^{VI}$ crystals for mid-IR and far-IR: Novel aspects in crystal growth," J. Cryst. Growth **310**, 1954–1960 (2008).
27. L. Isaenko, A. Yelisseyev, S. Lobanov, A. Panich, V. Vedenyapin, J. Smirnova, V. Petrov, J.-J. Zondy, and G. Knippels, "Characterization of LiInS$_2$ and LiInSe$_2$ single crystals for nonlinear optical applications," Mater. Res. Soc. Symp. Proc. **692**, 429–434 (2002).

28. L. Isaenko, A. Yelisseyev, J.-J. Zondy, G. Knippels, I. Thenot, and S. Lobanov, "Growth and characterization of single crystals of ternary chalcogenides for laser applications," Opto-Electron. Rev. **9**, 135–141 (2000); Proc. SPIE **4412**, 342–350 (2000).

29. L. Isaenko, A. Yelisseyev, S. Lobanov, V. Petrov, F. Rotermund, G. Slekys, and J.-J. Zondy, "LiInSe$_2$: a biaxial ternary chalcogenide crystal for nonlinear optical applications in the midinfrared," J. Appl. Phys. **91**, 9475–9480 (2002).

30. A. M. Panich, A. P. Yelisseyev, S. I. Lobanov, and L. I. Isaenko, "Comparative nuclear magnetic resonance study of as-grown and annealed LiInSe$_2$ ternary compounds," Hyperfine Interact. **159**, 199–203 (2004).

31. W. Hönle, G. Kühn, and H. Neumann, "Die Kristallstruktur von LiInSe$_2$," Z. Anorg. Allg. Chem. **543**, 161–168 (1986).

32. W. Hönle and G. Kühn, "Thermische Zersetzung von CuInSe$_2$, LiInSe$_2$ and LiInTe$_2$," J. Therm. Anal. **31**, 589–595 (1986).

33. H. J. Beister, S. Ves, W. Hönle, K. Syassen, and G. Kühn, "Structural phase transitions and optical absorption of LiInSe$_2$ under pressure," Phys. Rev. B **43**, 9635–9642 (1991).

34. B. Greuling, "Pressure-induced phase transformation in LiInSe$_2$," Cryst. Res. Technol. **22**, K27–K29 (1987).

35. H. J. Beister, W. Hönle, K. Syassen, and G. Kühn, "Pressure and temperature induced phase transitions in LiInSe$_2$," High Press. Res. **4**, 360–362 (1990).

36. R. Gratz, V. Sidorov, O. Tsiok, and B. Lorenz, "High-pressure phase diagram of LiInSe$_2$," High Press. Res. **8**, 445–447 (1991).

37. S. Ves, W. Hönle, and K. Syassen, "Raman scattering and phase changes of CuInSe$_2$ and LiInSe$_2$ at high pressure," High Press. Res. **9**, 36–40 (1992).

38. B. Lorenz, "High pressure Raman investigation of LiInSe$_2$ in the β-NaFeO$_2$ structure," J. Phys. Chem. Solids **58**, 399–402 (1997).

39. T. Kamijoh, T. Nozaki, and K. Kuriyama, "Dielectric constants and bond parameters of LiInSe$_2$ and LiGaSe$_2$," J. Appl. Phys. **53**, 761–763 (1982).

40. H. Neumann, "Bond ionicities and structural trends in some Li^{I}B^{III}C$_2^{VI}$ compounds," Cryst. Res. Technol. **21**, 1207–1212 (1986).

41. H. Sommer, D. W. Bullett, H. Neumann, and G. Kühn, "Valence band density of states in LiInSe$_2$," Phys. Status Solidi B **152**, K47–K50 (1989).

42. Yu. M. Basalaev, Yu. N. Zhuravlev, E. B. Kitova, and A. S. Poplavnoi, "Chemical bonding in isostructural Li-containing ternary chalcogenides," J. Struct. Chem. **48**, 1001–1005 (2007) [in Russian, Zhurnal Strukturnoi Khimii **48**, 1067–1071 (2007)].

43. L.-H. Li, J.-Q. Li, and L.-M. Wu, "Electronic structures and optical properties of wurtzite type LiBSe$_2$ (B=Al, Ga, In): A first-principles study," J. Solid State Chem. **181**, 2462–2468 (2008).

44. Y. Li, W. Fan, H. Sun, X. Cheng, P. Li, and X. Zhao, "First-principles study of the electronic, optical, and lattice dynamics properties of LiInSe$_2$ polymorph," J. Appl. Phys. **106**, 033704 (2009).

45. T. Ma, C. Yang, Y. Xie, L. Sun, W. Lv, R. Wang, C. Zhu, and M. Wang, "Electronic and optical properties of orthorhombic LiInS$_2$ and LiInSe$_2$: A density functional theory investigation," Comput. Mater. Sci. **47**, 99–105 (2009).

46. T. Kamijoh and K. Kuriyama, "Annealing effects on electrical properties of LiInSe$_2$," J. Appl. Phys. **52**, 1102–1103 (1981).

47. C. J. Smith and C. W. Lowe, "Stoichiometric effects on the optical properties of LiInSe$_2$," J. Appl. Phys. **66**, 5102–5104 (1989).

48. W. Hörig, H. Neumann, and G. Kühn, "The fundamental absorption edge of LiInSe$_2$," Phys. Status Solidi B **121**, K55–K58 (1984).

49. A. Eifler, V. Riede, S. Wenger, S. Weise, E. Nowak, and V. Krämer, "Optical band gap of LiInSe$_2$ single crystals,"

50. A. Eifler, V. Riede, J. Brückner, S. Weise, V. Krämer, G. Lippold, W. Schmitz, K. Bente, and W. Grill, "Band gap energies and lattice vibrations of the lithium ternary compounds LiInSe$_2$, LiInS$_2$, LiGaSe$_2$ and LiGaS$_2$," Jpn. J. Appl. Phys., Part 1 **39**, Suppl. 39–1, 279–281 (2000).

51. M. V. Kabanov, Yu. M. Andreev, V. V. Badikov, and P. P. Geiko, "Parametric frequency converters based on new nonlinear crystals," Russ. Phys. J. **46**, 835–846 (2003) [in Russian, Izv. Vyssh. Uchebn. Zaved. Fiz. **46**, 84–94 (2003)].

52. Yu. M. Andreev, V. V. Badikov, P. P. Geiko, S. G. Grechin, V. V. Efimenko, T. D. Efimenko, V. L. Panyutin, A. A. Tikhomirov, and A. V. Shaiduko, "Second harmonic generation of TEA CO$_2$ laser radiation in LiInSe$_2$," Atmos. Oceanic Opt. **17**, 115–120 (2004) [in Russian, Optika Atmosfery i Okeana **17**, 133–139 (2004)].

53. Yu. M. Andreev, P. P. Geiko, V. V. Badikov, V. L. Panyutin, G. S. Shevyrdyaeva, M. V. Ivaschenko, A. I. Karapuzikov, and I. V. Sherstov, "Parametric frequency converters with LiInSe$_2$, AgGaGeS$_4$, HgGa$_2$S$_4$ and Hg$_{0.65}$Cd$_{0.35}$Ga$_2$S$_4$ crystals," Proc. SPIE **5027**, 120–127 (2003).

54. O. Balachninaite, L. Petraviciute, M. Maciulevicius, V. Sirutkaitis, L. Isaenko, S. Lobanov, A. Yelisseyev, and J.-J. Zondy, "Absorptance and scattering losses measurements of the mid-infrared nonlinear crystals LiInSe$_2$ and LiInS$_2$ in the IR range," Ultragarsas **60**, 7–10 (2006).

55. O. Balachninaite, L. Petraviciute, M. Maciulevicius, V. Sirutkaitis, L. Isaenko, S. Lobanov, A. Yelisseyev, and J.-J. Zondy, "Characterization of the mid-infrared nonlinear crystals LiInSe$_2$ and LiInS$_2$ in the IR range," Proc. SPIE **6403**, 64031Y (2007).

56. O. Balachninaite, L. Petraviciute, M. Maciulevicius, V. Sirutkaitis, L. Isaenko, S. Lobanov, A. Yelisseyev, and J.-J. Zondy, "Optical characterization of the LiInS$_2$ and LiInSe$_2$ crystals," Proc. SPIE **6596**, 65961J (2007).

57. A. Eifler, V. Riede, S. Wenger, S. Weise, E. Nowak, D. Sprinz, G. Lippold, and W. Grill, "Infrared and Raman study of lattice vibrations of LiInSe$_2$ single crystals," Cryst. Res. Technol. **31**, Suppl. 31, 353–356 (1996).

58. P. Deus, H. A. Schneider, and U. Voland, "Estimation of the Debye temperature of diamond-like semiconducting compounds by means of the Lindemann rule," Cryst. Res. Technol. **16**, 941–948 (1981).

59. G. Kühn, E. Pirl, H. Neumann, and E. Nowak, "Heat capacity of LiInS$_2$, LiInSe$_2$, and LiInTe$_2$ between 200 and 550 K," Cryst. Res. Technol. **22**, 265–269 (1987).

60. A. P. Yelisseyev, A. S. Titov, L. I. Isaenko, S. I. Lobanov, K. M. Lyaounov, V. A. Gruzdev, S. G. Komarov, V. A. Drebushchak, V. Petrov, and J.-J. Zondy, "Thermal properties of the midinfrared nonlinear crystal LiInSe$_2$," J. Appl. Phys. **96**, 3659–3665 (2004).

61. E. Gmelin and W. Höhnle, "Anomalous lattice specific heat of LiInSe$_2$ at low temperatures," Thermochim. Acta **269–270**, 575–590 (1995).

62. T. Kamijoh, T. Nozaki, and K. Kuriyama, "Dielectric constant and its temperature dependence of LiInSe$_2$," Jpn. J. Appl. Phys. **19**, Suppl. 19-3, 395–397 (1980).

63. A. P. Yelisseyev, A. S. Titov, K. M. Lyapunov, V. A. Drebushchak, L. I. Isaenko, and S. I. Lobanov, "Thermal and thermo-optic parameters of LiInSe$_2$ single crystals," J. Cryst. Growth **275**, e1679–e1684 (2005).

64. C. M. Kachhava, *Solid State Physics* (Tata McGraw-Hill, 1990).

65. O. Bidault, S. Fossier, J. Mangin, P. Strimer, A. Yelisseyev, L. Isaenko, and S. Lobanov, "Study of the pyroelectricity in LiInS$_2$ crystal," Solid State Commun. **121**, 207–211 (2002).

66. Yu. M. Andreev, P. P. Geiko, and M. V. Kabanov, "New crystals for frequency-tunable lasers," Optoelectronics, Instrumentation and Data Processing **40**(5), 96–106 (2004) [in Russian, Avtometriya **40**(5), 119–133 (2004)].

67. J. J. Huang, Y. M. Andreev, G. V. Lanskii, A. V. Shaiduko, S. Das, and U. Chatterjee, "Acceptable composition-ratio variations of a mixed crystal for nonlinear laser device ap-

Cryst. Res. Technol. **31**, Suppl. 31, 233–236 (1996).

plications," Appl. Opt. **44**, 7644–7650 (2005).

68. V. V. Atuchin, Yu. M. Andreev, G. V. Lanskii, and A. V. Shaiduko, "Sellmeier equations for LiInS$_2$ and LiInSe$_2$," Proc. SPIE **6259**, 625917 (2006).

69. J.-J. Zondy, V. Vedenyapin, A. Yelisseyev, S. Lobanov, L. Isaenko, and V. Petrov, "LiInSe$_2$ nanosecond optical parametric oscillator," Opt. Lett. **30**, 2460–2462 (2005).

70. American National Standards Institute, *An American National Standard: IEEE Standard on Piezoelectricity, ANSI/IEEE Std 176-1987* (IEEE, 1988).

71. V. G. Dmitriev and D. N. Nikogosyan, "Effective nonlinearity coefficients for three-wave interactions in biaxial crystals of mm2 point group symmetry," Opt. Commun. **95**, 173–182 (1993).

72. M. V. Hobden, "Phase-matched second-harmonic generation in biaxial crystals," J. Appl. Phys. **38**, 4365–4372 (1967).

73. J. Q. Yao and T. S. Fahlen, "Calculations of optimum phase match parameters for the biaxial crystal KTiOPO$_4$," J. Appl. Phys. **55**, 65–68 (1984).

74. D. A. Roberts, "Simplified characterization of uniaxial and biaxial nonlinear optical crystals: a plea for standardization of nomenclature and conventions," IEEE J. Quantum Electron. **28**, 2057–2074 (1992).

75. F. Brehat and B. Wyncke, "Calculation of double-refraction walk-off angle along the phase-matching directions in nonlinear crystals," J. Phys. B **22**, 1891–1898 (1989).

76. J. Yao, W. Sheng, and W. Shi, "Accurate calculation of the optimum phase-matching parameters in three-wave interactions with biaxial nonlinear-optical crystals," J. Opt. Soc. Am. B **9**, 891–902 (1992).

77. W. Q. Zhang, "Optical parametric generation for biaxial crystals," Opt. Commun. **105**, 226–232 (1994).

78. V. I. Zadorozhnii, "Improved analytical method for calculating the parameters of phase-matched nonlinear-optical interactions in biaxial crystals," Opt. Commun. **176**, 489–501 (2000).

79. M. H. van der Mooren, Th. Rasing, and H. J. A. Bluyssen, "Determination of the type I phase matching angles and conversion efficiency in KTP," Appl. Opt. **34**, 934–937 (1995).

80. F. Rotermund and V. Petrov, "Femtosecond noncollinear optical parametric amplification in the mid-infrared range with 1.25 μm pumping," Jpn. J. Appl. Phys., Part 1 **40**, 3195–3200 (2001).

81. H. J. Liu, G. F. Chen, W. Zhao, Y. S. Wang, T. Wang, and S. H. Zhao, "Phase-matching analysis of noncollinear optical parametric process in nonlinear anisotropic crystals," Opt. Commun. **197**, 507–514 (2001).

82. W. Q. Zhang, "Group-velocity matching in the mixing of three noncollinear phase-matched waves for biaxial crystal," Opt. Commun. **221**, 191–197 (2003).

83. W. Q. Zhang, "Femtosecond optical parametric generation of noncollinear phase matching for a biaxial crystal," Appl. Opt. **42**, 5596–5601 (2003).

84. J.-J. Zondy, D. Touahri, and O. Acef, "Absolute value of the d_{36} nonlinear coefficient of AgGaS$_2$: prospect for a low-threshold doubly resonant oscillator-based 3:1 frequency divider," J. Opt. Soc. Am. B **14**, 2481–2497 (1997).

85. Yu. M. Andreev, V. V. Badikov, P. P. Geiko, V. V. Efimenko, T. D. Efimenko, M. V. Ivaschenko, A. I. Karapuzikov, V. L. Panyutin, and I. V. Sherstov, "Possibilities and experimental investigation of parametric frequency converters with LiInSe$_2$, AgGaGeS$_4$, HgGa$_2$S$_4$ and Hg$_{0.65}$Cd$_{0.35}$Ga$_2$S$_4$ crystals," in *Proceedings of the 6th Russian-Korean International Symposium on Science and Technology (KORUS-2002)* (IEEE, 2002), pp. 303–306.

86. J.-J. Zondy, "The effects of focusing in type-I and type-II difference-frequency generations," Opt. Commun. **149**, 181–206 (1998).

87. W. Chen, E. Poullet, J. Burie, D. Boucher, M. W. Sigrist, J.-J. Zondy, L. Isaenko, A. Yelisseyev, and S. Lobanov, "Widely tunable continuous-wave mid-infrared radiation (5.5–11 μm) by difference-frequency generation in LiInS$_2$ crystal," Appl. Opt. **44**, 4123–4129 (2005).

88. T.-B. Chu and M. Broyer, "Intracavity cw difference frequency generation by mixing three photons and using Gaussian laser beams," J. Phys. (France) **46**, 523–534 (1985).

89. V. Petrov, F. Noack, I. Tunchev, P. Schunemann, and K. Zawilski, "The nonlinear coefficient d_{36} of CdSiP$_2$," Proc. SPIE **7197**, 7197OM (2009).

90. K. L. Vodopyanov, J. P. Maffetone, I. Zwieback, and W. Rudermann, "AgGaS$_2$ optical parametric oscillator continuously tunable from 3.9 to 11.3 μm," Appl. Phys. Lett. **75**, 1204–1206 (1999).

91. G. Marchev, A. Tyazhev, V. Vedenyapin, D. Kolker, A. Yelisseyev, S. Lobanov, L. Isaenko, J.-J. Zondy, and V. Petrov, "Nd:YAG pumped nanosecond optical parametric oscillator based on LiInSe$_2$ with tunability extending from 4.7 to 8.7 μm," Opt. Express **17**, 13441–13446 (2009).

92. S. J. Brosnan and R. L. Byer, "Optical parametric oscillator threshold and linewidth studies," IEEE J. Quantum Electron. **15**, 415–431 (1979).

93. K. Kuriyama, A. Matsubara, T. Nozaki, and T. Kamijoh, "Preparation and characterization of the LiInSe$_2$ thin films," Nuovo Cimento Soc. Ital. Fis. **2D**, 1723–1727 (1983).

94. A. Tempel, B. Schumann, S. Mitaray, and G. Kühn, "LiInSe$_2$ thin epitaxial films on {111}A-oriented GaAs," Thin Solid Films **101**, 339–344 (1983); "LiInSe$_2$ thin epitaxial films on {111}A-oriented GaAs: Erratum," Thin Solid Films **105**, L88 (1983).

95. A. Tempel, B. Schumann, S. Mitaray, and G. Kühn, "Investigations of LiInSe$_2$ epitaxial layers on {100}- and {110}-oriented substrates with sphalerite structure by means of RHEED," Cryst. Res. Technol. **21**, 1429–1435 (1986).

96. K. Kuriyama, Y. Igarashi, F. Nakamura, and A. Okada, "Epitaxial growth of LiInSe$_2$ on {111}A oriented GaP by a hot wall technique," Appl. Phys. Lett. **48**, 1199–1201 (1986).

97. S. Wenger, V. Riede, A. Eifler, A. Lenz, S. Weise, E. Nowak, and B. Schumann, "Optical properties of thin films of LiInSe$_2$ prepared by pulsed laser deposition," Cryst. Res. Technol. **31**, Suppl. 31, 213–216 (1996).

98. K. Kuriyama and Y. Igarashi, "Electroluminescence from LiInSe$_2$–GaP heterodiodes," J. Appl. Phys. **56**, 1884–1885 (1984).

99. U.-C. Boehnke, H. Neumann, and G. Kühn, "Phase study of the system Cu$_{1-x}$Li$_x$InSe$_2$," J. Alloys Compd. **190**, L17–L18 (1992).

100. S. Weise, E. Nowak, A. Lenz, B. Schumann, and V. Krämer, "Investigations of the system LiInSe$_2$–CuInSe$_2$," J. Cryst. Growth **166**, 718–721 (1996).

101. S. Weise, E. Nowak, A. Eifler, B. Schumann, and V. Krämer, "Structural and physical properties of the system LiInSe$_2$–CuInSe$_2$," Cryst. Res. Technol. **31**, Suppl. 3, 797–800 (1996).

102. S. Mitaray, G. Kühn, B. Schumann, A. Tempel, W. Hörig, and H. Neumann, "Growth, structure and optical properties of Li$_x$Cu$_{1-x}$InSe$_2$ thin films," Thin Solid Films **135**, 251–256 (1986).

103. H. Sobotta, H. Neumann, S. Mitaray, V. Riede, and G. Kühn, "Infrared optical properties of Li$_x$Cu$_{1-x}$InSe$_2$ thin films," Cryst. Res. Technol. **22**, 1173–1178 (1987).

104. K. Takeya, Y. Takemoto, I. Kawayama, H. Murakami, T. Matsukawa, M. Yoshimura, Y. Mori, and M. Tonouchi, "Terahertz emission from coherent phonons in lithium ternary chalcopyrite crystals illuminated by femtosecond laser pulses," EPL **91**, 20004 (2010).